



# The poker-chip experiments of Gent and Lindley (1959) explained

Aditya Kumar, Oscar Lopez-Pamies \*

Department of Civil and Environmental Engineering, University of Illinois, Urbana-Champaign, IL 61801, USA

## ARTICLE INFO

### Keywords:

Elastomers  
Cavitation  
Fracture  
Strength  
Defects

## ABSTRACT

Despite being commonly credited with initiating the field of cavitation in elastomers, the famed poker-chip experiments of Gent and Lindley (1959) have yet to be fully explained. One likely reason for their elusiveness is that it had long been presumed that cavitation in elastomers was a phenomenon that could be explained solely on the basis of the elasticity of the elastomer at hand. Of late, full-field analyses and experiments carried out at high spatiotemporal resolution have impugned such a belief by indicating, instead, that cavitation in elastomers is first and foremost a fracture phenomenon. In that spirit, Kumar, Francfort, and Lopez-Pamies (2018) have introduced a comprehensive macroscopic phase-field theory for the nucleation and propagation of fracture in elastomers undergoing arbitrarily large quasistatic deformations. The purpose of this paper is to deploy this theory in order to explain in a detailed and quantitative manner the seminal poker-chip experiments of Gent and Lindley.

## 1. Introduction

At risk of being unfair,<sup>1</sup> we credit the poker-chip<sup>2</sup> experiments of Gent and Lindley (1957, 1959) in the 1950s as the work that jump-started fundamental investigations on the nucleation of internal cracks in elastomers subject to externally applied mechanical loads, a phenomenon now commonly referred to as *cavitation*.<sup>3</sup> Two schools of thought that emerged from their famed experiments merit explicit mention:

- i. *The elasticity view.* The first school of thought owes its genesis to Gent and Lindley (1959) themselves who to explain their experiments proposed to view the nucleation of internal cracks in elastomers as the purely elastic growth of the inherent defects that they invariably contain.
- ii. *The fracture view.* The second school of thought finds its origin in the work of Williams and Schapery (1965) who proposed to view nucleation of internal cracks in elastomers as the growth of their inherent defects by the creation of new surface – that is, by fracture – as dictated by the Griffith competition between the material bulk elastic energy and defect surface fracture energy (Griffith, 1921).

Because of its apparent agreement with some of the experimental poker-chip results and the beauty and simplicity of its most basic mathematical model – that is, the radially symmetric deformation of a single spherical cavity embedded in a homogeneous elastic

\* Corresponding author.

E-mail addresses: [akumar51@illinois.edu](mailto:akumar51@illinois.edu) (A. Kumar), [pamies@illinois.edu](mailto:pamies@illinois.edu) (O. Lopez-Pamies).

<sup>1</sup> Earlier experimental investigations of the same nature can be traced back to the works of Busse (1938) and Yerzley (1939) in the 1930s.

<sup>2</sup> The term “poker-chip” for such a type of experiments appears to have been coined after the work of Gent and Lindley; see Chapter II in the dissertation by Lindsey (1965).

<sup>3</sup> The term “cavitation” was introduced by Gent and Lindley (1957) themselves, who drew a comparison with the phenomenon of cavitation in liquids (Bull, 1956).

<https://doi.org/10.1016/j.jmps.2021.104359>

Received 17 October 2020; Received in revised form 6 December 2020; Accepted 5 February 2021

Available online 12 February 2021

0022-5096/© 2021 Elsevier Ltd. All rights reserved.

medium under remotely applied pressure – the elasticity view was intensely pursued by the mechanics community; see, e.g., the reviews contained in the works of [Horgan and Polignone \(1995\)](#), [Fond \(2001\)](#), and [Lopez-Pamies et al. \(2011a\)](#) put forth in the 1990s, 2000s, and 2010s. Following the seminal paper by [Ball \(1982\)](#), who formalized the analysis of [Gent and Lindley \(1959\)](#) and hinted at the many mathematical riches therein, the mathematics community too intensely pursued the view that cavitation was a purely elastic phenomenon. By contrast, in spite of delivering similar apparent agreement with some of the same experimental results, the fracture view did not receive nearly as much attention ([Gent, 1990](#); [Gent and Wang, 1991](#)).

In spite of the very many investigations of cavitation as a purely elastic phenomenon, it was only in 2015 that a direct comparison between theory and the original poker-chip experiments of [Gent and Lindley \(1959\)](#) was reported in the literature; see, however, [Stringfellow and Abeyaratne \(1989\)](#) for an earlier preliminary comparison. Precisely, with help of a general elastic cavitation criterion that had been developed a few years earlier ([Lopez-Pamies, 2009](#); [Lopez-Pamies et al., 2011a,b](#)), [Lefèvre et al. \(2015\)](#) carried out full-field simulations of the poker-chip experiments on the unfilled elastomers studied by [Gent and Lindley \(1959\)](#) under the premise that their mechanical behavior was nonlinear elastic and that their underlying defects at which cavitation could initiate were vacuous and their spatial distribution was random and isotropic. Their results indicated that, while the nonlinear elasticity of the elastomers was important, cavitation as reported by [Gent and Lindley \(1959\)](#) was first and foremost a fracture process. This was essentially because the local stretches around the defects at which cavitation presumably initiated from far exceeded the elastic limit of the elastomers being tested, which therefore ought to accommodate their growth by fracture. The conclusions pointed to by [Lefèvre et al. \(2015\)](#) were later corroborated by [Poulain et al. \(2017, 2018\)](#), who carried out experiments in the spirit of those reported by [Gent and Park \(1984\)](#) involving two neighboring filler particles but at the much higher resolutions of 1  $\mu\text{m}$  in space and 67 ms in time.

Instructed by the findings of [Lefèvre et al. \(2015\)](#) and [Poulain et al. \(2017, 2018\)](#), as well as by the plethora of experimental results accumulated in the literature over more than 80 years on elastomers with pre-existing cracks ([Busse, 1934](#); [Rivlin and Thomas, 1953](#); [Thomas, 1994](#)), [Kumar et al. \(2018a\)](#) have recently put forth a comprehensive theory of fracture – regularized, of phase-field type – that models the nucleation and propagation of fracture in elastomers undergoing arbitrarily large quasistatic deformations on equal footing. In a nutshell, the theory posits that *nucleation of fracture*

- in the bulk – that is, cavitation – is governed by the strength of the elastomer,
- from large<sup>4</sup> pre-existing cracks is governed by the Griffith competition between its bulk elastic energy and surface fracture energy,
- from boundary points, be them smooth or sharp, and small pre-existing cracks is governed by the interaction among the strength, the bulk elastic energy, and the surface fracture energy of the elastomer,

while *propagation of fracture*

- is, akin to nucleation from large pre-existing cracks, also governed by the Griffith competition between the bulk elastic energy and surface fracture energy of the elastomer.

Having validated in [Kumar et al. \(2018a,b\)](#) the predictions of the theory directly with the experiments of [Poulain et al. \(2017, 2018\)](#), the purpose of this work is to deploy the theory to explain the seminal poker-chip experiments of [Gent and Lindley \(1959\)](#) in a detailed and quantitative manner.

The organization of the paper is as follows. We begin in Sections 2 and 3 by summarizing the experiments of [Gent and Lindley \(1959\)](#) and by recalling the fracture theory of [Kumar et al. \(2018a\)](#). In Section 4, we present the calibration of the elasticity, the strength, and the critical elastic energy release rate of the elastomer labeled D by [Gent and Lindley \(1959\)](#), the elastomer for which they presented the most complete set of results and hence for which we carry out the comparisons here. In Section 5, based on those calibrated material inputs, we then present 3D full-field simulations of the experiments as predicted by the theory and compare them directly with all the three types of results reported by [Gent and Lindley \(1959\)](#), namely, the force-deformation response of the poker-chip specimens, the post-mortem images of their midplanes illustrating the geometry and spatial distribution of the internally nucleated cracks, and the critical applied forces at which cracks approximately first nucleate. We conclude this work by recording a number of final comments in Section 6.

At the close of this Introduction, it is important to emphasize that the explanation of the poker-chip experiments of [Gent and Lindley \(1959\)](#) put forth in this paper is of a macroscopic or top-down nature. Indeed, the theory of [Kumar et al. \(2018a\)](#) is a macroscopic theory of fracture. Its material inputs are the elasticity of the elastomer at hand, its strength, and its critical energy release rate, as obtained from measurements carried out at length scales of micrometers or larger. At present, in spite of the existence of a plurality of hypotheses ([Lake and Thomas, 1967](#); [Raphaël and de Gennes, 1992](#); [Creton and Ciccotti, 2016](#)), little remains known about the extent to which different types of molecular bonds – e.g., carbon-carbon bonds, crosslinks, chain entanglements, van der Waals bonds – contribute to the creation of new macroscopic fracture surfaces in elastomers. Even from a more modest continuum mesoscopic perspective, like that suggested by [Williams and Schapery \(1965\)](#), it remains unclear how one should model defects – from either geometric or constitutive points of view – and whether a Griffith-like competition between bulk and surface energies would be an accurate description of their eventual growth into macroscopic fracture.

<sup>4</sup> “Large” refers to large relative to the characteristic size of the inherent microscopic defects in the elastomer under investigation. By the same token, “small” refers to sizes that are of the same order or just moderately larger than the sizes of the inherent defects. The characteristic size of the inherent defects in most standard elastomers ranges from a few nanometers to a few tens of nanometers ([Gent, 1990](#); [Valentin et al., 2010](#); [Poulain et al., 2017](#)).

## 2. A summary of the poker-chip experiments of Gent and Lindley (1959)

*Types of elastomers.* Gent and Lindley (1959) carried out experiments on eight different types of elastomers, which they labeled A through H; see the appendix in their paper. Except for the elastomer F, which was made of a butadiene-styrene copolymer, all were natural rubber with different crosslink densities. Moreover, elastomers A, B, and C were filled with carbon black particles at volume fractions  $c = 0.18, 0.14,$  and,  $0.07,$  respectively.

*Characterization of the initial elasticity of the elastomers.* Assuming incompressibility, the Young's modulus  $E$  of all the elastomers was determined from indentation hardness measurements (Gent, 1958). By design, they featured a wide spectrum of mean values ranging from  $E = 5.884$  MPa for the stiffest elastomer A to  $E = 0.932$  MPa for the softest elastomer H.

*The geometry of the poker-chip specimens.* Fig. 1 shows a schematic of the poker-chip specimens. They comprised a disk – the “poker-chip” – made of the elastomer of interest,  $D = 2$  cm in initial diameter and ranging from  $H = 0.040$  cm to  $H = 0.980$  cm in initial thickness, bonded on its top and bottom to metal cylindrical fixtures by means of cement during the vulcanization process. The diameter-to-thickness ratio of the elastomer disks, a key geometrical quantity in dictating how fracture nucleates and propagates, was varied thus from roughly  $D/H = 50$  to  $D/H = 2$ .

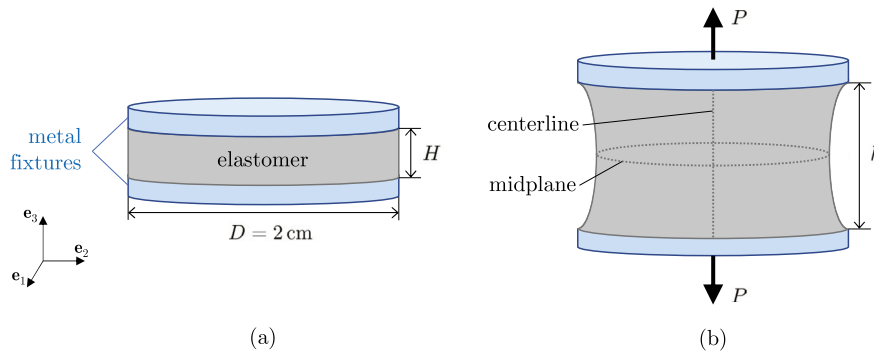


Fig. 1. Schematic of the poker-chip experimental setup of Gent and Lindley (1959) in (a) the undeformed configuration and in (b) a deformed configuration at an applied deformation  $h$  and corresponding tensile force  $P$ . The initial diameter of the elastomer disks – the “poker-chips” – was fixed at  $D = 2$  cm, while their initial thicknesses were varied from  $H = 0.040$  cm to  $H = 0.980$  cm.

*The poker-chip tests.* Once fabricated, the poker-chip specimens were mounted on a Hounsfield tensometer and then subjected to a tensile deformation that was applied quasistatically at a rate of about their initial thickness  $H$  per minute, that is,  $\dot{h}/H \approx 0.017$  s<sup>-1</sup>.

The vast majority of tests were carried out all the way until complete failure of the specimen. A number of tests, however, were stopped at various select forces and the elastomer disks cut open across their midplane for visual inspection of the internally nucleated cracks; see Fig. 1(b). Some tests were also carried out cyclically in the sense that the specimen was loaded up to some applied deformation, unloaded, and then reloaded up to a larger applied deformation than that reached during the first loading.

Gent and Lindley (1959) measured both the force  $P$  in the poker-chip specimens and their deformation  $h$  as read directly off the Hounsfield tensometer. They reported these quantities normalized by the initial area and thickness of the specimens, that is,  $S = 4P/(\pi D^2)$  and  $\lambda = h/H$ ; see Fig. 1. As elaborated below in Section 4.1, however, the compliance of the Hounsfield tensometer was not negligible and therefore needs to be taken into account in order to determine the actual deformation  $h$  of the poker-chips. Denoting by  $k_T$  the stiffness of the Hounsfield tensometer and by  $h_T$  its deformation reading, the actual deformation of the poker-chips can be deduced from the relation  $h = h_T - P/k_T$ . The calibration process presented below in Section 4.1 indicates that  $k_T = 19.3$  kN/cm.

*The three types of reported results.* The first of the three different types of results reported by Gent and Lindley (1959) comprises the force-deformation response of the poker-chip specimens up to a large force ( $S = 5.88$  MPa) but not all the way until their complete failure (see Fig. 1 in their paper); partial data for the average force at the complete failure of the specimens is included in Table 1 of their paper.

The second type of results is the post-mortem images of the midplane of specimens cut open right after reaching the normalized force  $S = 2.75$  MPa (see Fig. 4 in their paper).

Finally, Gent and Lindley (1959) also reported the values of a critical stress  $S'$ , as a function of the poker-chip initial thickness  $H$  and the elastomer Young's modulus  $E$  (see Figs. 6 and 7 in their paper), which they defined as the value of the normalized force  $S$  at the first local maximum in the force-deformation response of the specimens and referred to as the “cracking stress”. They surmised that  $S'$  signaled the first nucleation of cracks. As elaborated below in Section 4.2, however, it turns out that  $S'$  bounds from above the actual critical value of  $S$ , say  $S^*$ , at which the first nucleation of cracks occurs. In the sequel, for clarity, we shall refer to  $S^*$  as the “cracking stress” and to  $S'$  as the “local-maximum stress”.

The bulk of the above-outlined three types of results presented by Gent and Lindley (1959) pertain exclusively to the elastomer D; the other seven types of elastomers were stated to exhibit similar behaviors.

### 3. The fracture theory of Kumar, Francfort, and Lopez-Pamies (2018)

Consider an elastomer occupying an open bounded domain  $\Omega_0 \subset \mathbb{R}^3$ , with boundary  $\partial\Omega_0$  and outward unit normal  $\mathbf{N}$ , in its undeformed and stress-free configuration at time  $t = 0$ . Material points are identified by their initial position vector  $\mathbf{X} \in \Omega_0$ . At a later time  $t \in (0, T]$ , due to an externally applied deformation  $\bar{\mathbf{y}}(\mathbf{X}, t)$  on a part  $\partial\Omega_0^D$  of the boundary and a nominal traction  $\bar{\mathbf{t}}(\mathbf{X}, t)$  on the complementary part  $\partial\Omega_0^N = \partial\Omega_0 \setminus \partial\Omega_0^D$ , the position vector  $\mathbf{X}$  of a material point moves to a new position specified by

$$\mathbf{x} = \mathbf{y}(\mathbf{X}, t),$$

where  $\mathbf{y}$  is a mapping from  $\Omega_0$  to the current configuration  $\Omega(t)$ , also contained in  $\mathbb{R}^3$ . We write the deformation gradient as

$$\mathbf{F}(\mathbf{X}, t) = \frac{\partial \mathbf{y}}{\partial \mathbf{X}}(\mathbf{X}, t) = \nabla \mathbf{y}(\mathbf{X}, t).$$

In response to the same externally applied mechanical stimuli that result in the above-described deformation, cracks can also nucleate and propagate in the elastomer. Those are described in a regularized fashion by the order parameter or phase field

$$z = z(\mathbf{X}, t)$$

taking values in  $[0, 1]$ . Precisely,  $z = 1$  identifies regions of the sound elastomer, whereas  $z = 0$  identifies regions of the elastomer that have been fractured.

Now, write the stored-energy function describing the elasticity of the elastomer in the form

$$\mathcal{W}(\mathbf{F}) = W(\mathbf{F}) + \kappa g(\mathbf{F}), \tag{1}$$

take its strength to be characterized by the strength surface<sup>5</sup>

$$F(\mathbf{S}) = 0 \tag{2}$$

in the space of first Piola–Kirchhoff stresses  $\mathbf{S}$ , and denote by

$$G_c \tag{3}$$

its critical elastic energy release rate.<sup>6</sup>

Then, according to the theory of Kumar et al. (2018a), the deformation field  $\mathbf{y}(\mathbf{X}, t)$  and phase field  $z(\mathbf{X}, t)$  at any material point  $\mathbf{X} \in \Omega_0$  and time  $t \in [0, T]$  are determined by the system of coupled partial differential equations (PDEs)

$$\begin{cases} \text{Div} \left[ (z^2 + \eta_W) \frac{\partial W}{\partial \mathbf{F}}(\nabla \mathbf{y}) + (z^2 + \eta_\kappa) \kappa \frac{\partial g}{\partial \mathbf{F}}(\nabla \mathbf{y}) \right] = \mathbf{0}, & \mathbf{X} \in \Omega_0 \times [0, T] \\ \det \nabla \mathbf{y}(\mathbf{X}, t) > 0, & \mathbf{X} \in \Omega_0 \times [0, T] \\ \mathbf{y}(\mathbf{X}, t) = \bar{\mathbf{y}}(\mathbf{X}, t), & \mathbf{X} \in \partial\Omega_0^D \times [0, T] \\ \left[ (z^2 + \eta_W) \frac{\partial W}{\partial \mathbf{F}}(\nabla \mathbf{y}) + (z^2 + \eta_\kappa) \kappa \frac{\partial g}{\partial \mathbf{F}}(\nabla \mathbf{y}) \right] \mathbf{N} = \bar{\mathbf{t}}(\mathbf{X}, t), & \mathbf{X} \in \partial\Omega_0^N \times [0, T] \end{cases} \tag{4}$$

and

$$\begin{cases} \text{Div} [\varepsilon k(\dot{z}) \nabla z] = \frac{8}{3} z (W(\nabla \mathbf{y}) + \kappa g(\nabla \mathbf{y})) - \frac{4}{3} c_e(\mathbf{X}, t) - \frac{k(\dot{z})}{2\varepsilon} & \text{if } 0 < z(\mathbf{X}, t) < 1 \text{ and } \dot{z}(\mathbf{X}, t) \neq 0, \quad (\mathbf{X}, t) \in \Omega_0 \times [0, T] \\ \text{Div} [\varepsilon k(\dot{z}) \nabla z] \geq \frac{8}{3} z (W(\nabla \mathbf{y}) + \kappa g(\nabla \mathbf{y})) - \frac{4}{3} c_e(\mathbf{X}, t) - \frac{k(\dot{z})}{2\varepsilon} & \text{if } z(\mathbf{X}, t) = 1 \text{ or } \dot{z}(\mathbf{X}, t) = 0, \quad (\mathbf{X}, t) \in \Omega_0 \times [0, T] \\ \text{Div} [\varepsilon k(\dot{z}) \nabla z] \leq \frac{8}{3} z (W(\nabla \mathbf{y}) + \kappa g(\nabla \mathbf{y})) - \frac{4}{3} c_e(\mathbf{X}, t) - \frac{k(\dot{z})}{2\varepsilon} & \text{if } z(\mathbf{X}, t) = 0, \quad (\mathbf{X}, t) \in \Omega_0 \times [0, T] \\ \nabla z \cdot \mathbf{N} = 0, & (\mathbf{X}, t) \in \partial\Omega_0 \times [0, T] \end{cases} \tag{5}$$

with  $\mathbf{y}(\mathbf{X}, 0) \equiv \mathbf{X}$  and  $z(\mathbf{X}, 0) \equiv 1$ , where

$$k(\dot{z}) = \begin{cases} G_c & \text{if } \dot{z} \leq 0 \\ 0 & \text{if } \dot{z} > 0 \end{cases} \tag{6}$$

with  $\dot{z}(\mathbf{X}, t) := \partial z(\mathbf{X}, t) / \partial t$ , and where  $\varepsilon > 0$  is a regularization or localization length, and  $c_e(\mathbf{X}, t)$  is a driving force whose specific constitutive prescription, spelled out in Section 3.1 below, depends on the particular form of the strength surface (2).

<sup>5</sup> When an elastomer is subjected to a state of monotonically increasing *uniform* but otherwise *arbitrary* stress, fracture will nucleate from one or more of its inherent defects at a critical value of the applied stress. The set of all such critical stresses defines a surface in stress space. In terms of the first Piola–Kirchhoff stress tensor  $\mathbf{S}$ , that surface is given by (2).

<sup>6</sup> Here, it is important to emphasize that standardized tests to measure the material constants in any stored-energy function (1) of choice and the critical energy release rate (3) for a given elastomer of interest have long been available and can be readily carried out with conventional equipment. By contrast, it is difficult to carry out experiments that probe the entire space of uniform stresses in order to measure its entire strength surface (2). Most of the strength data available in the literature is narrowly restricted to uniaxial tensile strength  $s_{ts}$  when  $\mathbf{S} = \text{diag}(s_{ts}, 0, 0)$  with  $s_{ts} > 0$ , hydrostatic strength  $s_{hs}$  when  $\mathbf{S} = \text{diag}(s_{hs}, s_{hs}, s_{hs})$  with  $s_{hs} > 0$ , and, to a lesser extent, biaxial tensile strength  $s_{bs}$  when  $\mathbf{S} = \text{diag}(s_{bs}, s_{bs}, 0)$  with  $s_{bs} > 0$ ; see, e.g., Smith (1964), Smith and Rinde (1969), Dickie and Smith (1969), Kawabata (1973), Gent and Mars (2013), and Poulain et al. (2017).

For convenience, the remarks and subsections that follow summarize the key theoretical and practical features of the fracture theory (4)–(5). The interested reader is referred to Kumar et al. (2018a,b) and Kumar and Lopez-Pamies (2020) for a complete account.

**Remark 1.** *The form of the stored-energy function (1) and associated parameters  $\eta_W$  and  $\eta_\kappa$  in (4).* The parameter  $\kappa$  in (1) is a non-negative material parameter that serves to measure the compressibility of the elastomer under investigation. Specifically, it is defined such that in the limit as  $\kappa \rightarrow +\infty$ , the elastomer is incompressible and its stored-energy function reduces to

$$\mathcal{W}(\mathbf{F}) = \begin{cases} W(\mathbf{F}) & \text{if } \det \mathbf{F} = 1 \\ +\infty & \text{otherwise} \end{cases}.$$

Most stored-energy functions available in the literature conform to (1). An example to be used in all the simulations presented in this work is given by the isotropic stored-energy function (Lopez-Pamies, 2010)

$$\mathcal{W}(\mathbf{F}) = \sum_{r=1}^2 \frac{3^{1-\alpha_r}}{2\alpha_r} \mu_r (I_1^{\alpha_r} - 3^{\alpha_r}) - \sum_{r=1}^2 \mu_r \ln J + \frac{\kappa}{2} (J - 1)^2 \tag{7}$$

with

$$I_1 = \text{tr}(\mathbf{F}^T \mathbf{F}), \quad J = \det \mathbf{F},$$

where  $\mu_r$  and  $\alpha_r$  are material parameters and where one can readily identify that

$$W(\mathbf{F}) = \sum_{r=1}^2 \frac{3^{1-\alpha_r}}{2\alpha_r} \mu_r (I_1^{\alpha_r} - 3^{\alpha_r}) - \sum_{r=1}^2 \mu_r \ln J, \quad g(\mathbf{F}) = \frac{1}{2} (J - 1)^2, \tag{8}$$

and that  $\kappa = \Lambda + 2\mu/3 - 2(\alpha_1\mu_1 + \alpha_2\mu_2)/3$  in terms of the first and second Lamé constants  $\Lambda$  and  $\mu = \mu_1 + \mu_2$ .

The associated parameters  $\eta_W$  and  $\eta_\kappa$  in (4) stand for small positive numbers that serve to aid the numerical tractability of the vanishingly small stiffness of the regions of the elastomer that have undergone fracture. When dealing with nearly incompressible elastomers, the compressibility parameter  $\kappa$  is typically  $10^3$  to  $10^4$  larger than the rest of material parameters describing the elasticity of the elastomer. Thus, to ensure that the fractured regions are of vanishingly small stiffness, the parameter  $\eta_\kappa$  needs to be chosen in general much smaller than  $\eta_W$ . In the simulations presented below for nearly incompressible natural rubber, we set  $\eta_\kappa = (\mu/\kappa)\eta_W$ , where, again,  $\mu$  stands for the second Lamé constant or initial shear modulus of the elastomer.

**Remark 2.** *The toughness function (6).* The first branch in the toughness function (6) states that fracture nucleation from large pre-existing cracks as well as fracture propagation occur according to the critical energy release rate  $G_c$  of the elastomer. The second branch, on the other hand, states that fracture is a purely dissipative and irreversible process.

It is well known that certain types of elastomers – most notably, natural rubber – can crystallize when subject to large stretches. Such a strain crystallization can occur in the bulk or localize near finitely deformed crack fronts. The apparent critical energy release rate of the regions that strain-crystallize is expected to be substantially larger than the nominal value  $G_c$  of the amorphous regions and, in addition, to be anisotropic; see, e.g., Busse (1934), Hamed et al. (1996), Zhang et al. (2009), and Rong et al. (2016). We will come back to this important point further below in Section 4.3.

Recent experimental evidence has also revealed that internally nucleated cracks in elastomers may self-heal (Poulain et al., 2017, 2018). The theory (4)–(5) can describe such a healing process by setting a positive value, say  $0 < k_H \leq G_c$ , in the second branch of the toughness function (6), as opposed to just 0; see Section 3.2 in Kumar et al. (2018a) for relevant details and Francfort et al. (2019) for a “sharp-theory” perspective on the concept of a healing toughness  $k_H$ . For the purposes of this paper, it suffices to adopt the standard assumption of fracture irreversibility, thus our choice of toughness function (6).

**Remark 3.** *The localization length  $\varepsilon$ .* The localization length  $\varepsilon$  in Eqs. (5) is just a regularization parameter that is void of any further physical meaning. In principle, one should undertake the task of passing to the limit as  $\varepsilon \searrow 0$ , showing that the Eqs. (4)–(5) converge in some reasonable topology to a putative set of “equations” that models both nucleation and propagation of sharp cracks in elastomers. Although numerical evidence points to the existence of such a set of equations, for now, passing to the limit remains a tall order because of mathematical technicalities. In practice, it suffices to select a value for  $\varepsilon$  that is smaller than the smallest characteristic length scale in the structural problem at hand. For the poker-chip experiments of interest here (see Fig. 1), this implies that we must select  $\varepsilon \ll H$ .

**Remark 4.** *Numerical method of solution.* The construction of numerical solutions for the PDEs (4)–(5) poses two major challenges. Those are the selection of an appropriate space discretization capable of dealing with large deformations and the near incompressibility typical of elastomers and the selection of an appropriate solver for the nonlinear algebraic equations resulting from the discretization capable of dealing with the large changes in the deformation field  $\mathbf{y}(\mathbf{X}, t)$  locally in space and time that can ensue from the nucleation of fracture. Kumar et al. (2018a) introduced in Section 4 of their work a robust finite-element (FE) scheme that addresses these challenges by making use of a non-conforming FE discretization of low order due to Crouzeix and Raviart (1973), suitably modified with a stabilization term (Babuska and Zlamal, 1973; Hansbo and Larson, 2003; Xu and Henao, 2011), and an implicit gradient flow solver (Behrman, 1998; Neuberger, 2010) combined with a staggered strategy. All the simulations presented in this paper are generated with that scheme.

3.1. The constitutive prescription for the driving force  $c_e(\mathbf{X}, t)$

Physically,  $c_e(\mathbf{X}, t)$  stands for a driving force that represents the macroscopic manifestation of the presence of the inherent microscopic defects in the elastomer. It is hence the quantity through which the strength (2) of the elastomer enters the theory. To see this, as expounded in Section 4 of Kumar and Lopez-Pamies (2020), note that when the elastomer under investigation is subjected to a state of uniform stress, say a uniform first Piola–Kirchhoff stress  $\mathbf{S}$ , Eqs. (4) are trivially satisfied while Eqs. (5) predict that the phase field  $z$  ceases to be identically 1 whenever the right-hand side of (5)<sub>1</sub> vanishes, that is, whenever the algebraic equation

$$F^\epsilon(\mathbf{S}) = 2(W(\mathbf{F}) + \kappa g(\mathbf{F})) - c_e - \frac{3G_c}{8\epsilon} = 0 \tag{9}$$

is satisfied, where  $\mathbf{F}$  is given in terms of the applied uniform stress  $\mathbf{S}$  by the implicit relation  $\mathbf{S} = \partial W(\mathbf{F})/\partial \mathbf{F} + \kappa \partial g(\mathbf{F})/\partial \mathbf{F}$ . By then choosing a constitutive prescription for the driving force  $c_e$  such that the phase field  $z$  localizes near 0 right after ceasing to be 1, Eq. (9) defines the strength surface described by the fracture theory (4)–(5) for the elastomer at hand.

Now, because of the near incompressibility of the elastomers that Gent and Lindley (1959) tested, nucleation of fracture in all their poker-chip experiments always occurs at sites where the stress is not far from a state of purely hydrostatic stress when  $\mathbf{S} = s\mathbf{I} = \text{diag}(s, s, s)$  with  $s > 0$ . For the purposes of this paper, following the blueprint provided in Section 4 of Kumar and Lopez-Pamies (2020) for constructing driving forces  $c_e$  and as further elaborated in Section 4.2 below, it then suffices to set<sup>7</sup>

$$c_e(\mathbf{X}, t) = -z \left( \frac{3^{9/4} G_c \kappa}{8\epsilon s_{\text{hs}}} \right) \frac{J - 1}{I_1^{5/4}}, \tag{10}$$

where  $s_{\text{hs}}$  stands for the hydrostatic strength of the nearly incompressible elastomer at hand, that is, the critical value  $s_{\text{hs}}$  of the stress  $s$  at which fracture nucleates in the elastomer when this is subjected to states of uniform stress of the form  $\mathbf{S} = s\mathbf{I}$  with  $s > 0$ . Indeed, upon direct use of the prescription (10) and of the functions (8) chosen here to describe the elasticity of elastomers, it is straightforward to deduce that the evaluation of the strength surface (9) along states of purely hydrostatic stress  $\mathbf{S} = s\mathbf{I}$  reduces to

$$F^\epsilon(s\mathbf{I}) = \sum_{r=1}^2 \frac{3\mu_r}{\alpha_r} (\lambda^{2\alpha_r} - 1) - 2 \sum_{r=1}^2 \mu_r \ln \lambda^3 + \kappa (\lambda^3 - 1)^2 + \frac{3G_c \kappa (\lambda^3 - 1)}{8s_{\text{hs}}\epsilon \lambda^{5/2}} - \frac{3G_c}{8\epsilon} = 0, \tag{11}$$

where  $\lambda$  is given in terms of the applied uniform hydrostatic stress  $s$  by the implicit relation  $s = \sum_{r=1}^2 \mu_r (\lambda^{2\alpha_r - 1} - \lambda^{-1}) + \kappa \lambda^2 (\lambda^3 - 1)$ . For nearly incompressible elastomers when  $\kappa \gg \mu_1, \mu_2$ , this last relation admits an explicit inversion in favor of  $\lambda$ . The result reads

$$\lambda = 1 + \frac{s}{3\kappa} + O\left(\frac{1}{\kappa^2}\right).$$

Making use of this last result allows to finally deduce that (11) simplifies to

$$F^\epsilon(s\mathbf{I}) = \frac{3G_c}{8\epsilon s_{\text{hs}}} (s - s_{\text{hs}}) + O\left(\frac{1}{\kappa}\right) = 0$$

and hence that the strength surface (9) described by the fracture theory (4)–(5) with driving force (10) reduces *identically* (to leading order in the limit as  $\kappa \rightarrow +\infty$ ) to the strength surface of the given elastomer (2) for states of purely hydrostatic stress:

$$F^\epsilon(s_{\text{hs}}\mathbf{I}) = F(s_{\text{hs}}\mathbf{I}) = 0,$$

this for any value of the localization length  $\epsilon$ .

3.2. The fracture theory (4)–(5) as a generalization of the variational phase-field approach to fracture

There are two natural manners in which the fracture theory (4)–(5) can be thought of. The first one, put forth in Kumar et al. (2018a), is as a generalization of the phase-field regularization (Bourdin et al., 2008)

$$\begin{aligned} \mathbf{y} = \bar{\mathbf{y}}_m(\mathbf{X}) \text{ on } \partial\Omega_0^D \\ 0 \leq z \leq z_{m-1} \leq 1 \end{aligned} \quad \mathcal{E}^\epsilon(\mathbf{y}, z) := \int_{\Omega_0} z^2 \mathcal{W}(\mathbf{F}(\mathbf{y})) \, d\mathbf{X} - \int_{\partial\Omega_0^N} \bar{\mathbf{t}}(\mathbf{X}, t_m) \cdot \mathbf{y} \, d\mathbf{X} + \frac{3G_c}{8} \int_{\Omega_0} \left( \frac{1-z}{\epsilon} + \epsilon \nabla z \cdot \nabla z \right) \, d\mathbf{X} \tag{12}$$

of the celebrated variational theory of brittle fracture of Francfort and Marigo (1998), which in turn is nothing more than the mathematical statement of Griffith’s fracture postulate in its general form of energy cost–benefit analysis; in this last expression, we have made use of the notation  $\bar{\mathbf{y}}_m(\mathbf{X}) = \bar{\mathbf{y}}(\mathbf{X}, t_m)$  and  $z_m(\mathbf{X}) = z(\mathbf{X}, t_m)$ , where  $t_m$  is any given discrete time  $t_m \in \{0 = t_0, t_1, \dots, t_n, t_{n+1}, \dots, t_N = T\}$ .

Precisely, the generalization amounts:

- i. to considering the Euler–Lagrange equations of the phase-field regularization (12) – and *not* the variational principle (12) itself – as the primal model,

<sup>7</sup> The denominator  $I_1^{5/4}$  in (10) ensures that the driving force effectively vanishes ahead of crack fronts and hence that it does not intervene in their propagation. The exponent 5/4 is chosen in order to enforce that the phase field  $z$  localizes near 0 right after ceasing to be 1, as desired.

- ii. to adding the driving force  $c_e$  in the Euler–Lagrange equation governing the evolution of the phase field  $z$ , and
- iii. to removing the irreversibility constraint on the phase field  $z$  by introducing the toughness function (6) with two branches, one to describe fracture, the other to describe healing.

The power of the variational phase-field formulation (12) lies in the fact that it describes the Griffith *propagation* of cracks in elastomers subject to arbitrary quasistatic loading conditions in a manner such that can be numerically handled with a standard FE method of solution. Provided that the driving force  $c_e$  is prescribed appropriately, the fracture theory (4)–(5) describes the same Griffith propagation of cracks as the variational formulation (12); see Subsection 4.2.4 in Kumar and Lopez-Pamies (2020).

The shortfall of the variational formulation (12) is that it cannot describe *nucleation* of fracture in general. This is because it does not account for one of the basic ingredients required to model fracture nucleation: the strength of the material. Its generalization (4)–(5) has the ability to describe fracture nucleation in elastomers subject to arbitrary quasistatic loading conditions thanks to taking into account the strength of the material via the additional driving force  $c_e$ ; see Sections 3 and 4 in Kumar and Lopez-Pamies (2020).

### 3.3. The fracture theory (4)–(5) as a phase transition

Alternatively, as laid out in Kumar et al. (2018b), the fracture theory (4)–(5) can also be thought of as a phase-transition of Ginzburg–Landau (or Allen–Cahn) type. Precisely, within the framework of configurational forces put forth by Fried and Gurtin (1994) and Gurtin (1996), Eqs. (4)<sub>1</sub> and (5)<sub>1–3</sub> can be thought of as the balance of Newtonian forces that drive the deformation:

$$\text{Div } \mathbf{S} = \mathbf{0},$$

and the balance of configurational forces that drive the nucleation and propagation of fracture:

$$\begin{cases} \text{Div } \mathbf{C} + c_1 + c_e(\mathbf{X}, t) = 0 & \text{if } 0 < z < 1 \text{ and } \dot{z} \neq 0 \\ \text{Div } \mathbf{C} + c_1 + c_e(\mathbf{X}, t) \geq 0 & \text{if } z = 1 \text{ or } \dot{z} = 0 \\ \text{Div } \mathbf{C} + c_1 + c_e(\mathbf{X}, t) \leq 0 & \text{if } z = 0 \end{cases}.$$

Here,

$$\mathbf{S}(\mathbf{X}, t) = (z^2 + \eta_W) \frac{\partial W}{\partial \mathbf{F}}(\nabla \mathbf{y}) + (z^2 + \eta_\kappa) \kappa \frac{\partial g}{\partial \mathbf{F}}(\nabla \mathbf{y})$$

stands for the first Piola–Kirchhoff stress tensor, conjugate to the deformation gradient  $\mathbf{F}$ , while

$$\begin{cases} c_1(\mathbf{X}, t) = -2z(W(\nabla \mathbf{y}) + \kappa g(\nabla \mathbf{y})) + \frac{3k(\dot{z})}{8\epsilon} \\ \mathbf{C}(\mathbf{X}, t) = \frac{3}{4} \epsilon k(\dot{z}) \nabla z \end{cases}$$

stand for the configurational *internal* force  $c_1$  and the configurational stress  $\mathbf{C}$ , conjugate to the configurational variables  $z$  and  $\nabla z$ , at any material point  $\mathbf{X} \in \Omega_0$  and time  $t$ . In this setting, we note that the driving force  $c_e$  is referred to as the configurational *external* force.

*The driving force  $c_e$  as a configurational external force.* As emphasized at the close of the Introduction, the fracture theory (4)–(5) is a *macroscopic* theory. As such, it accounts not for the explicit presence of the inherent microscopic defects in the material but only for their macroscopic manifestation, the strength, via the driving force  $c_e$ . Guided by the calculations presented in the Appendix of Kumar et al. (2018a), we interpret such a macroscopic manifestation as an *external* force. Those calculations of Kumar et al. (2018a) were aimed at gaining insight into the microscopic origins of the driving force  $c_e$  by comparing the predictions of the macroscopic fracture theory (4)–(5) for the nucleation of fracture in a homogeneous ball of elastomer subjected to hydrostatic pressure with the nucleation of fracture in a ball of the same elastomer wherein a microscopic defect – a small vacuous spherical cavity at the ball’s origin – was accounted for explicitly. Two observations emerged. First, by appropriately calibrating the driving force  $c_e$ , the macroscopic view of the problem could describe the same nucleation as the microscopic view accounting for the defect. Second, in the microscopic view there was a concentration of elastic and surface energy around the deforming defect that obviously was not present in the macroscopic view. While this localized energy is internal to the material system with the defect, its effect can be accounted for as an external force in the macroscopic view.

### 3.4. A comment on other phase-field models of fracture for elastomers

Starting with the work of Del Piero et al. (2007) some 15 years ago, an increasing number of authors have put forth numerical implementations and/or extensions of the standard variational phase-field approach to fracture in the context of quasistatic finite elastic deformations (Bourdin et al., 2008) with the objective of describing fracture in elastomers. For instance, Miehe and Schänzel (2014) and Henao et al. (2016) presented 2D numerical implementations of the so-called<sup>8</sup> classical AT<sub>2</sub> phase-field model alongside

<sup>8</sup> The terminology AT<sub>2</sub> refers to the fact that the regularization of the surface area of cracks makes use of the form  $S_\epsilon(z) = ((1-z)^2/\epsilon + \epsilon \nabla z \cdot \nabla z)/2$  introduced in Ambrosio and Tortorelli (1992). The shortcomings of this regularization have been recently highlighted in Tanné et al. (2018).

some illustrative simulations. Hesch and Weinberg (2014) and Wu et al. (2016) made use of modified  $AT_2$  phase-field models in which only a certain “tensile” part  $\mathcal{W}^+(\mathbf{F})$  of the stored-energy function  $\mathcal{W}(\mathbf{F})$  is active in the fracture process and presented as well illustrative 2D simulations. Following a derivation *à la* configurational forces, Talamini et al. (2018) proposed an  $AT_2$ -type phase-field model where the stored-energy function  $\mathcal{W}(\mathbf{F})$  accounts for the energy contribution due to bond stretching at large macroscopic deformations and compared its predictions with experiments due to Hocine et al. (2002) on an SBR elastomer. Li and Bouklas (2019) presented a phase-field model in the same spirit as that of Talamini et al. (2018), but did so using a hybrid displacement–pressure formulation that permitted them to handle the near incompressibility of elastomers. More recently, Mandal et al. (2020) have proposed a phase-field model that incorporates some of the features of cohesive fracture models.

A common feature in all of the above-mentioned phase-field models is that they describe the evolution of the phase field ( $z$  in our notation) as a competition between bulk elastic energy and regularized surface fracture energy. When calibrated appropriately, they are thus capable of accurately describing the Griffith *propagation* of cracks in elastomers subject to arbitrary quasistatic loading conditions.

By the same token, however, they are not capable of describing fracture *nucleation* in elastomers at large.<sup>9</sup> As discussed at length and demonstrated with simulations of the Gent–Park experiments of Poulain et al. (2017) in Kumar et al. (2018a), this is because this class of materials are nearly incompressible and hence prone to feature regions where the hydrostatic part of the stress is very large while, at the same time, the elastic energy is comparatively negligible (because the strain is negligible). Since fracture often nucleates in such regions of high hydrostatic stress but negligible elastic energy, this implies that the stress – and not just the bulk elastic energy – must enter the competition that describes the evolution of the phase field. Again, the fracture theory (4)–(5) accounts for this required additional competition via the external driving force  $c_e$ .

#### 4. Calibration of the three material inputs entering the theory

We now proceed with the calibration of the three material inputs – again, the stored-energy function  $\mathcal{W}(\mathbf{F})$ , the strength surface  $F(S)$ , and the critical energy release rate  $G_c$  – entering the governing Eqs. (4)–(5) for the elastomer under investigation here, the so-labeled elastomer D by Gent and Lindley (1959).

We emphasize that out of all the experimental results – extracted from a total of thirty different experiments with thirty different thicknesses in the range  $H \in [0.040, 0.980]$  cm – presented by Gent and Lindley (1959) for elastomer D, only partial information from three of them is used to carry out the calibration process. Specifically, as elaborated in the next three subsections, the force-deformation response of the thickest poker-chip specimen with  $H = 0.980$  cm is used to calibrate the stored-energy function  $\mathcal{W}(\mathbf{F})$  describing the elasticity of the elastomer. The value  $S^* = 1.80$  MPa of the “cracking stress” extracted from the force-deformation response of a very thin poker-chip specimen with initial thickness  $H = 0.056$  cm is used to calibrate its hydrostatic strength  $s_{hs}$ . Finally, the length of the crack in the post-mortem image of the midplane in the specimen with  $H = 0.370$  cm is used to calibrate its critical energy release rate  $G_c$ .

##### 4.1. Calibration of the stored-energy function $\mathcal{W}(\mathbf{F})$

Gent and Lindley (1959) reported

$$E = 1.765 \text{ MPa} \quad (13)$$

as the Young’s modulus for elastomer D. They did not include, however, direct data for its bulk modulus  $K$  or its elastic response at finite deformations. Nevertheless, from the separate thorough experiments on natural rubber by Wood and Martin (1964) we can confidently set

$$K = 2.20 \text{ GPa}$$

and hence deduce that the Lamé constants  $\Lambda$  and  $\mu$  of elastomer D are

$$\Lambda = \frac{3K(3K - E)}{9K - E} = 2.20 \text{ GPa} \quad \text{and} \quad \mu = \frac{3KE}{9K - E} = 0.588 \text{ MPa}. \quad (14)$$

Moreover, the elastic response of elastomer D at finite deformations can be extracted from the force-deformation response of the thickest poker-chip specimen ( $H = 0.980$  cm) that Gent and Lindley (1959) plotted in Fig. 1 of their paper, since that specimen, presumably, did only deform without fracturing. To do so, we make use of the stored-energy function (7) to describe the elasticity of the elastomer<sup>10</sup> and then determine its five material parameters  $\mu_1, \mu_2, \alpha_1, \alpha_2, \kappa$  by fitting the force-deformation response obtained from a purely elastic simulation of the experiment, subject to the constraints imposed by the Lamé constants (14), namely,

$$\mu_1 + \mu_2 = \mu = 0.588 \text{ MPa} \quad \text{and} \quad \kappa + \frac{2}{3}(\alpha_1\mu_1 + \alpha_2\mu_2) = \Lambda + \frac{2}{3}\mu = 2201 \text{ MPa}.$$

<sup>9</sup> In the footsteps of Amor et al. (2009), some of the above-mentioned phase-field models impart physical meaning to the localization length ( $\epsilon$  in our notation) by tying up its value to the uniaxial tensile strength of the elastomer at hand. This does allow them to at least be able to describe nucleation of fracture under the simple stress state of uniaxial tension.

<sup>10</sup> Among other possible choices, we make use of the stored-energy function (7) here because of its demonstrated capabilities to describe and predict the elastic response of a variety of elastomers, including natural rubber, together with its robustness to determine its five material parameters from small sets of experimental data; see, e.g., Section 2 in Lopez-Pamies (2010) and Section 4 in Leonard et al. (2020).

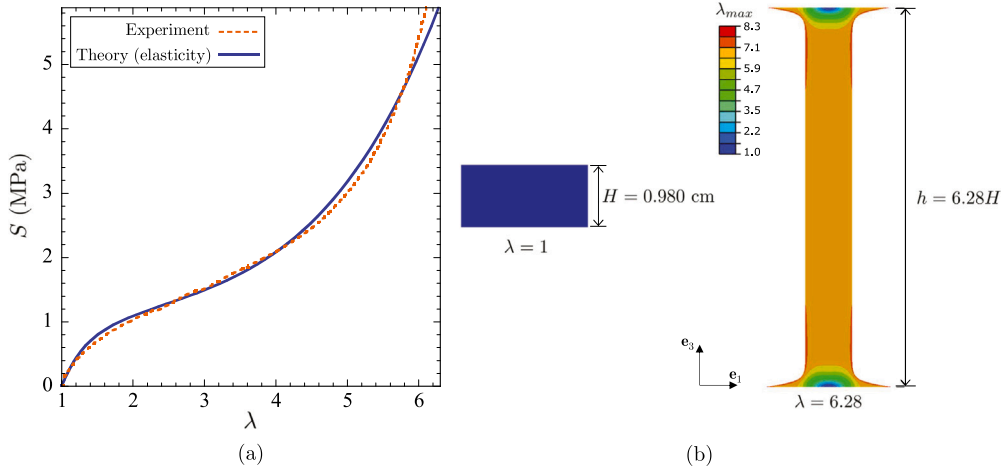


Fig. 2. Comparison between the experimental data and its elastic simulation for the poker-chip test on elastomer D with initial thickness  $H = 0.980$  cm. The simulation makes use of the stored-energy function (7) with material parameters (15) to characterize the elasticity of the elastomer. (a) The normalized force  $S = 4P/(\pi D^2)$  in the specimen as a function of the normalized applied deformation  $\lambda = h/H$ . (b) Contour plot of the maximum local stretch  $\lambda_{max}$  in the most deformed configuration of the specimen, when  $\lambda = 6.28$ , as determined from the simulation.

Such a fitting process yields the values

$$\mu_1 = 0.583 \text{ MPa}, \quad \mu_2 = 0.005 \text{ MPa}, \quad \alpha_1 = 0.650, \quad \alpha_2 = 2.725, \quad \kappa = 2.20 \text{ GPa}. \quad (15)$$

Fig. 2(a) compares the resulting force-deformation response (solid line) with the experimental data (dotted line). For completeness, Fig. 2(b) also shows the contour plot of the maximum stretch  $\lambda_{max}$  over the deformed configuration of the specimen at the largest applied deformation  $\lambda = h/H = 6.28$ ; for visual reference, the undeformed configuration of the specimen, when  $\lambda = h/H = 1$ , is also included alongside. Two observations are in order. The stored-energy function (7) with material parameters (15) seems to describe the elasticity of elastomer D for all deformations, small and large, fairly accurately. Furthermore, elastomer D can sustain stretches of at least  $\lambda_{max} = 8.3$  in its bulk without fracturing.

**Remark 5.** As alluded to above, the compliance of the Hounsfield tensometer utilized by Gent and Lindley (1959) to carry out their poker-chip tests was not negligible. This can be readily seen from the results presented in Fig. 3. There, we reproduce the initial force-deformation response prior to fracture from the poker-chip test on elastomer D with initial thickness  $H = 0.190$  cm plotted in Fig. 2 of their paper (dotted line) and compare it with the theoretical results from two different purely elastic simulations. The first theoretical result (dashed line) corresponds to a simulation where the tensometer is taken to be infinitely stiff ( $k_T = +\infty$ ) so that the

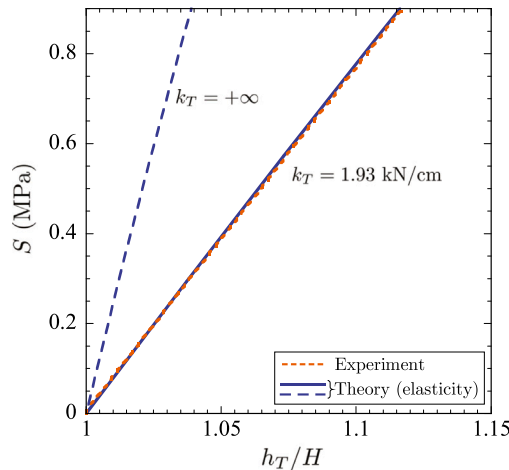


Fig. 3. The normalized force  $S = 4P/(\pi D^2)$  in the poker-chip specimen of elastomer D with initial thickness  $H = 0.190$  cm as a function of the normalized applied deformation  $h_T/H$ , where  $h_T$  is read directly off the tensometer. The dotted line corresponds to the experimental data prior to the occurrence of fracture, while the solid and dashed lines correspond to simulations where the stiffness of the tensometer is  $k_T = 19.3 \text{ kN/cm}$  and  $k_T = +\infty$ , respectively.

deformation  $h$  of the specimen can be identified with the deformation  $h_T$  read off the tensometer. On the other hand, the second theoretical result (solid line) corresponds to a simulation where the tensometer is taken to have a finite constant stiffness  $k_T = 19.3$  kN/cm so that the actual deformation  $h$  of the specimen is given by  $h = h_T - P/k_T$ . Both simulations pertain to an elastomer with the Lamé constants (14) of elastomer D. It is plain from these comparisons that the deformation of the tensometer must be taken into account in order to deduce the correct deformation  $h$  of the specimens. All the values presented for  $h$  in this paper account for the finite stiffness  $k_T = 19.3$  kN/cm of the tensometer.

4.2. Calibration of the strength surface  $F(S)$

No direct experimental data on the strength of elastomer D was included by Gent and Lindley (1959). From its conventional synthesis process, nevertheless, it is reasonable to assume that its strength surface is isotropic and hence that it admits the representation

$$F(S) = \hat{F}(s_1, s_2, s_3) = 0 \tag{16}$$

in terms of the eigenvalues  $s_1, s_2, s_3$  of the Biot stress  $S^{(1)} = (S^T R + R^T S)/2$ ,  $R$  denoting the rigid rotation stemming from the polar decomposition  $F = RU$  of the deformation gradient.

More critically, the hydrostatic strength  $s_{hs}$  of elastomer D can be extracted from the force-deformation response of the thinnest poker-chip specimen ( $H = 0.056$  cm) that Gent and Lindley (1959) plotted in Fig. 1 of their paper, in particular, from the value of the “cracking stress”  $S^*$  in that response. To determine that value, we first reproduce theoretically the experiment under the premise that the elastomer is only capable of deforming elastically – its elasticity being characterized by the above-calibrated stored-energy function (7) with material parameters (15) – then confront the resulting force-deformation response with the experimental data, and finally identify the value of the normalized force  $S$  at which the experimental data first deviates from the theoretical purely elastic response as the “cracking stress”  $S^*$ . Fig. 4 shows the result of that exercise from which we deduce that  $S^* = 1.80$  MPa.

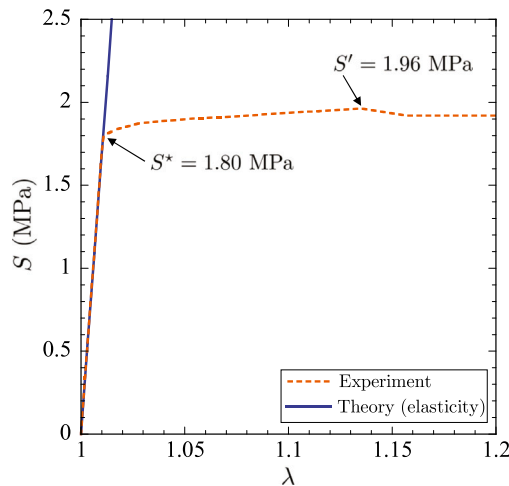


Fig. 4. Comparison between the experimental data and its elastic simulation for the poker-chip test on elastomer D with initial thickness  $H = 0.056$  cm. The point at which the elastic simulation deviates from the experiment identifies the “cracking stress”  $S^* = 1.80$  MPa, that is, the critical value of normalized force  $S$  at which cracks first nucleate. Note that  $S^*$  is somewhat smaller than the “local-maximum stress”  $S' = 1.96$  MPa defined by Gent and Lindley (1959) as the value of  $S$  at the first local maximum in the force-deformation response.

**Remark 6.** Albeit indirect, the above-outlined procedure of determining the “cracking stress”  $S^*$  from the point at which the force-deformation response measured experimentally for a given poker-chip specimen deviates from its theoretical purely elastic response is expected to be very robust. This is because the deformations are locally small in the elastomer – and hence its elastic response is accurately described by any model that linearizes properly according to the given Lamé constants, in the present case, (14) – prior to the nucleation of cracks. At the first nucleation of cracks, furthermore, the geometric softening afforded by their sudden appearance is expected to manifest itself as a marked softening of the force-deformation response of the specimen. As shown by Fig. 4, the onset of such a marked softening need not correspond to a local maximum as Gent and Lindley (1959) speculated. Thus, in general,  $S' \geq S^*$ .

Having determined  $S^* = 1.80$  MPa as the “cracking stress”, the second and final step to extract the hydrostatic strength  $s_{hs}$  of elastomer D consists in inspecting the local stress fields predicted by the elastic simulation over the specimen precisely at  $S = S^* = 1.80$  MPa. To that end, Fig. 5 presents contour plots of the principal Biot stresses  $s_1, s_2, s_3$  over the undeformed configuration of the specimen at  $S = S^* = 1.80$  MPa; the corresponding applied deformation is  $\lambda = h/H = 1.011$ . As expected

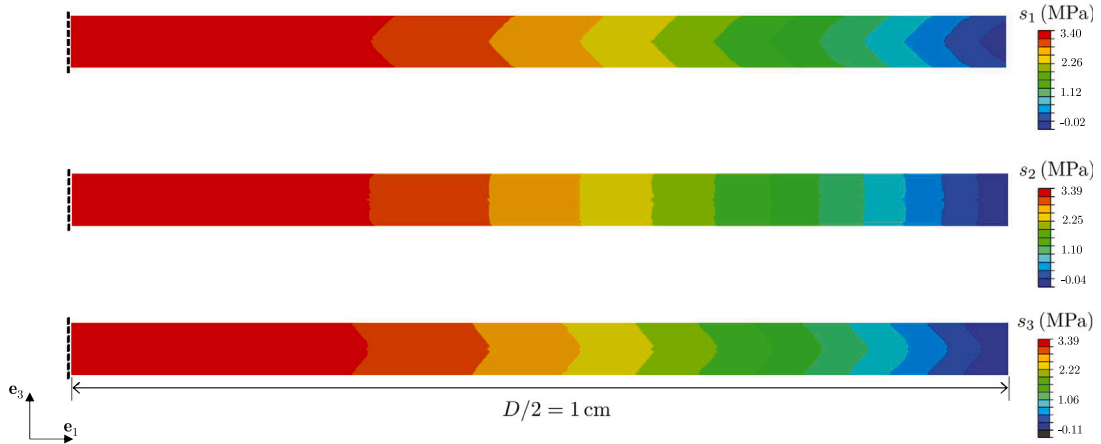


Fig. 5. Computed contour plots of the three principal Biot stresses  $s_1, s_2, s_3$  in the poker-chip specimen of elastomer D with initial thickness  $H = 0.056$  cm at the normalized force  $S = 4P/(\pi D^2) = S^* = 1.80$  MPa; the plots are shown only over half of the specimen for better visualization.

from the nearly incompressibility of the elastomer, the first Piola–Kirchhoff stress  $\mathbf{S}$  throughout the central region of the specimen – where the nucleation of cracks is believed to occur first based on post-mortem images – is roughly uniform and purely hydrostatic. Quantitatively, it is roughly equal to  $\mathbf{S} = \text{diag}(3.4, 3.4, 3.4)$  MPa. From this full-field analysis, we deduce that the hydrostatic strength of elastomer D is about

$$s_{hs} = 3.4 \text{ MPa.}$$

**Remark 7.** At this point, it is important to recognize that strength data is inherently stochastic. This is because the strength at a macroscopic material point  $\mathbf{X}$  depends on the nature of the underlying microscopic defects from which fracture initiates, and this is known to exhibit a stochastic spatial variation in any given piece of elastomer. Accordingly, the value of the hydrostatic strength  $s_{hs}$  of elastomer D is not expected to be constant but, instead, to take spatially random heterogeneous values in some range  $[s_{hs}^{min}, s_{hs}^{max}]$  throughout the domain  $\Omega_0$  that the piece of elastomer under investigation occupies. The comparisons between the theory (4)–(5) and the experiments presented below suggest that the range

$$s_{hs} \in [2.4, 3.4] \text{ MPa} \tag{17}$$

is descriptive of elastomer D. This corresponds to an average value of  $s_{hs} = 2.9$  MPa with  $\pm 15\%$  variation.

Lower and upper bounds for the uniaxial tensile strength  $s_{ts}$  and the biaxial tensile strength  $s_{bs}$  can also be estimated from the force-deformation response of the thickest poker-chip specimen ( $H = 0.980$  cm), already analyzed above in Fig. 2, in conjunction with separate experiments on natural rubber available in the literature (Smith, 1964; Kawabata, 1973). The latter indicate that, at room temperature and under loads that are applied quasistatically, natural rubber with Young’s modulus of about (13) – and hence similar crosslink densities as that of elastomer D – can typically sustain stretches in the ranges  $\lambda_{ts} \in [7.5, 9]$  in uniaxial tension and  $\lambda_{bs} \in [6, 7.5]$  in biaxial tension before fracturing. These values are consistent with the local stretches found in the simulation of the thickest poker-chip experiment shown in Fig. 2(b). Making use of the stored-energy function (7) with material parameters (15), we can then estimate that the uniaxial and biaxial tensile strengths of elastomer D are in the ranges

$$s_{ts} \in [7.5, 15] \text{ MPa} \quad \text{and} \quad s_{bs} \in [8.5, 21] \text{ MPa.} \tag{18}$$

These correspond to average values  $s_{ts} = 11.3$  MPa and  $s_{bs} = 14.8$  MPa with variations of  $\pm 33\%$  and  $\pm 42\%$ , respectively. Note that these values are significantly larger than those of the hydrostatic strength (17).

Having identified (17) and (18) for a mere three points on the strength surface (16) of elastomer D, in principle, one would have to continue identifying more points from experiments in order to have an accurate enough description of such a surface in the entire  $(s_1, s_2, s_3)$ -space. It turns out, however, that those three strength data points are all we need for our purposes here, especially the data point for the hydrostatic strength  $s_{hs}$ . This is because the nucleation of fracture in all of the poker-chip specimens tested by Gent and Lindley (1959) can be shown – via simulations – to always occur at sites where the stress state is not only in the first octant of the  $(s_1, s_2, s_3)$ -space, but narrowly confined in the region defined by the cone<sup>11</sup>

$$\mathcal{R} = \left\{ (s_1, s_2, s_3) : \sqrt{s_1^2 + s_2^2 + s_3^2 - s_1 s_2 - s_1 s_3 - s_2 s_3} - \frac{|\delta - 1|}{1 + 2\delta} (s_1 + s_2 + s_3) \leq 0, \quad \delta = 1.2 \right\} \tag{19}$$

<sup>11</sup> Precisely, the greatest difference between the largest, say  $s_1$ , and the smallest, say  $s_3$ , principal Biot stresses at a fracture nucleation point among all the poker-chip specimens tested by Gent and Lindley (1959) is just 20%, that is,  $s_1 = 1.2s_3$ . This happens at the cracks nucleated farthest from the center in the thinnest poker-chip specimen ( $H = 0.040$  cm). The greatest difference between the smallest principal Biot stress  $s_3$  and the intermediate one  $s_2$  is a mere 4%, that is,  $s_2 = 1.04s_3$ . This happens at the crack nucleated at the center in the poker-chip specimen with initial thickness  $H = 0.565$  cm.

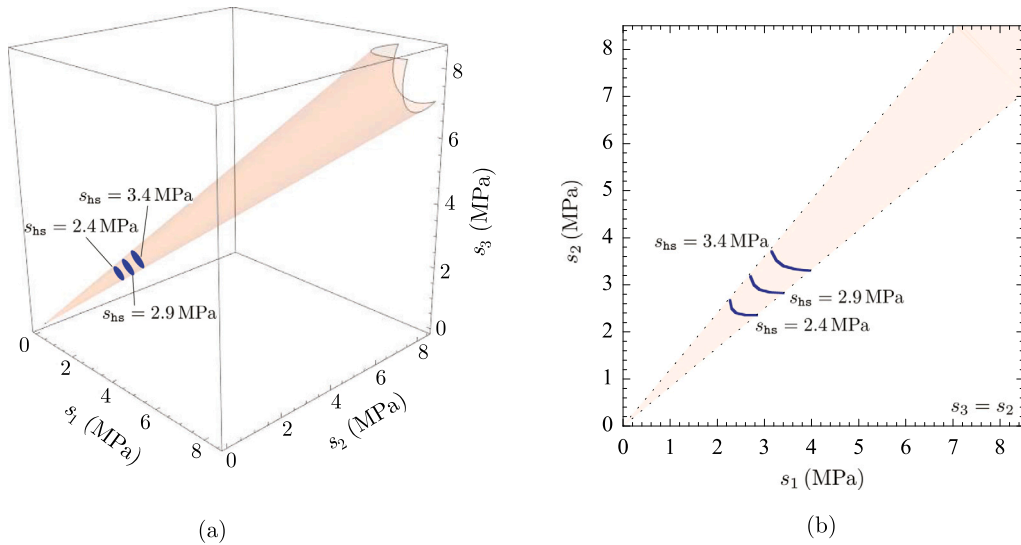


**Fig. 6.** The strength surface (20) for elastomer D. The results correspond to elastic material parameters (15), critical energy release rate (21), localization length  $\epsilon = 30 \mu\text{m}$ , three values of the hydrostatic strength  $s_{hs}$  in the range (17), and are shown confined within the envelope defined by the cone (19); the three surfaces are shown in blue, while the confining envelope is marked in light orange. (a) Plot of the surfaces in the space of principal Biot stresses  $(s_1, s_2, s_3)$ . (b) Plot of the surfaces in the projected  $(s_1, s_2)$ -space with  $s_3 = s_2$ .

around the purely hydrostatic line  $s_1 = s_2 = s_3$ . Ergo, only the part of the strength surface (16) that lies within (19) is relevant here.

Because of this restriction, it suffices to make use of the simple external driving force (10) – as opposed to more elaborate external driving forces such as that introduced by Kumar and Lopez-Pamies (2020) – in the governing Eqs. (4)–(5). The choice (10) implies that the strength surface surmised for elastomer D is given by

$$\hat{F}(s_1, s_2, s_3) = 2\hat{W}(\lambda_1, \lambda_2, \lambda_3) + \left( \frac{3^{5/4} \kappa (\lambda_1 \lambda_2 \lambda_3 - 1)}{s_{hs} (\lambda_1^2 + \lambda_2^2 + \lambda_3^2)^{5/4}} - 1 \right) \frac{3G_c}{8\epsilon} = 0, \tag{20}$$

where  $\lambda_1, \lambda_2, \lambda_3$  are defined implicitly in terms of the principal Biot stresses  $s_1, s_2, s_3$  by the system of three nonlinear algebraic equations

$$s_i = \frac{\partial \hat{W}}{\partial \lambda_i}(\lambda_1, \lambda_2, \lambda_3) \quad i = 1, 2, 3$$

with

$$\hat{W}(\lambda_1, \lambda_2, \lambda_3) = \sum_{r=1}^2 \frac{3^{1-\alpha_r}}{2\alpha_r} \mu_r [(\lambda_1^2 + \lambda_2^2 + \lambda_3^2)^{\alpha_r} - 3^{\alpha_r}] - \sum_{r=1}^2 \mu_r \ln(\lambda_1 \lambda_2 \lambda_3) + \frac{\kappa}{2} (\lambda_1 \lambda_2 \lambda_3 - 1)^2.$$

Fig. 6 presents plots of the strength surface (20), with elastic material parameters (15), critical energy release rate (21), and localization length  $\epsilon = 30 \mu\text{m}$ , for the minimum  $s_{hs} = 2.4 \text{ MPa}$ , the average  $s_{hs} = 2.9 \text{ MPa}$ , and the maximum  $s_{hs} = 3.4 \text{ MPa}$  values of the hydrostatic strength in the stochastic range (17). Fig. 6(a) shows the entire strength surfaces in the space of principal Biot stresses  $(s_1, s_2, s_3)$  within the envelope (19), highlighted in light orange. Fig. 6(b) shows the strength surfaces in the projected  $(s_1, s_2)$ -space with  $s_3 = s_2$ . The main observation here is that the strength surface (20) traces roughly an interpolation between the hydrostatic strength  $s_{hs}$  and values of the uniaxial  $s_{ts}$  and biaxial  $s_{bs}$  tensile strengths in the ranges (18).

### 4.3. Calibration of the critical energy release rate $G_c$

No experimental data on the critical energy release rate of elastomer D was provided by Gent and Lindley (1959). Nevertheless, from the classical experimental campaign and analysis of Lake and Lindley (1965) and Lake and Thomas (1967) on natural and synthetic rubbers, we know that, absent viscous dissipation and strain crystallization, the critical energy release rate of elastomer D is about  $G_c = 50 \text{ N/m}$ .

In view of the rate  $\dot{h}/H \approx 0.017 \text{ s}^{-1}$  of deformation applied to the poker-chip specimens, however, viscous dissipation is expected to be present (Kumar et al., 2017) in all of the tests reported by Gent and Lindley (1959). While the theory of Kumar et al. (2018a) does not account for viscous dissipation, it can address its toughening effect on the propagation of fracture by utilizing a value of the critical energy release rate that is larger than the actual value, *de facto* lumping together the contributions from the dissipations due to viscous deformations and the creation of new surfaces into an effective  $G_c$ . Guided by the length of the crack in the post-mortem image of the midplane in the specimen with  $H = 0.370 \text{ cm}$  (see Fig. 11) and the experiments of Lake and Lindley (1965) on a natural

rubber of similar characteristics to those of elastomer D (see the data for natural rubber gum vulcanizate A in Figs. 2 and 3 in their paper), we therefore set

$$G_c = G_c^a = 1000 \text{ N/m} \tag{21}$$

for the critical energy release rate of elastomer D in its amorphous state.

Strain crystallization is also expected to occur in all of the tests reported by Gent and Lindley (1959), especially within localized regions around the fronts of the nucleated cracks that reach sufficiently large stretches. While the theory of Kumar et al. (2018a) does not account for strain crystallization either, it can also address its toughening effect on the propagation of fracture by again utilizing a value of the critical energy release rate that is larger than the value (21) for its amorphous state. According again to the classical experimental data of Lake and Lindley (1965), values of an “effective” critical energy release rate accounting for both viscous dissipation and strain crystallization can be as large as 10000 N/m.

Now, owing to numerous investigations (Busse, 1934; Flory, 1947; Tosaka et al., 2004; Huneau, 2011; Guilié et al., 2015; Rong et al., 2016; Sotta and Albouy, 2020) since the seminal work of Katz (1925) in the 1920s, it is well established that crystallization in natural rubber under *uniaxial tension* starts occurring when the applied stretch reaches values in the range  $\lambda_{ut}^{c1} \in [3.5, 4]$ . The more the rubber is stretched, the larger the content of rubber that crystallizes. It is only recently, however, that experiments on crystallization under more complex states of deformation, such as equal and unequal biaxial stretch, have started to appear in the literature (Beurrot et al.; Chen et al., 2019). Those indicate that the degree of crystallinity that can be achieved is generally lesser the more the deformation state deviates from uniaxial tension towards equal biaxial tension.

Here, we model the bare essence of the phenomenon of strain crystallization by setting the critical energy release rate of elastomer D to be given by a piecewise constant function that switches its value from (21) first to  $G_c = G_c^{c1} = 2500 \text{ N/m}$  and then to  $G_c = G_c^{c2} = 10000 \text{ N/m}$  at increasingly larger deformations; as elaborated in Appendix A, the choice of these specific values is supported by comparisons with experiments. Precisely, consistent with the above-referenced experiments – in particular, those presented by Chen et al. (2019) in Fig. 6(a) of their paper – we take  $G_c = G_c^a = 1000 \text{ N/m}$  for deformations in the set

$$\mathcal{A} = \left\{ (I_1, I_2) : I_1, I_2 \in \mathbb{R}^+ \text{ such that either } \frac{I_2}{I_1} - 0.762I_1 + 9.22 > 0 \text{ and } \frac{I_2}{I_1^2} + 0.0129I_1 - 0.42 < 0 \text{ or } \frac{I_2}{I_1} - 0.2515I_1 + 0.1477 > 0 \right\}, \tag{22}$$

and  $G_c = G_c^{c1} = 2500$  and  $G_c = G_c^{c2} = 10000 \text{ N/m}$  for deformations in the sets

$$C_1 = \left\{ (I_1, I_2) : I_1, I_2 \in \mathbb{R}^+, (I_1, I_2) \notin \mathcal{A} \text{ such that either } \frac{I_2}{I_1} - 0.829I_1 + 16.71 > 0 \text{ and } \frac{I_2}{I_1^2} + 0.0095I_1 - 0.402 < 0 \text{ or } \frac{I_2}{I_1} - 0.254I_1 + 0.97 > 0 \right\} \tag{23}$$

and

$$C_2 = \{ (I_1, I_2) : I_1, I_2 \in \mathbb{R}^+ \text{ such that } (I_1, I_2) \notin \mathcal{A} \text{ and } (I_1, I_2) \notin C_1 \}, \tag{24}$$

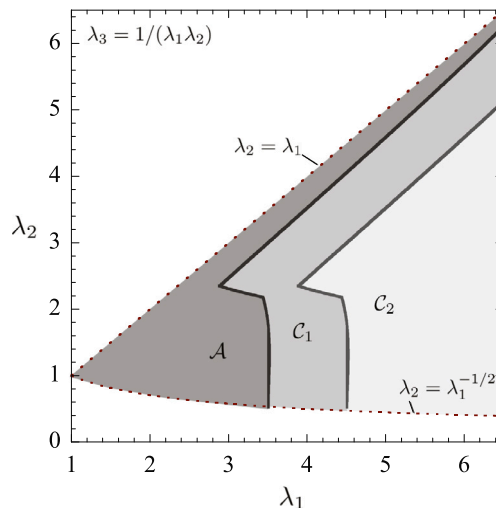


Fig. 7. The sets of deformations (22), (23), and (24) where elastomer D is taken to be in its amorphous ( $\mathcal{A}$ ) and strain-crystallized ( $C_1$  and  $C_2$ ) states, plotted in the projected space of principal stretches  $(\lambda_1, \lambda_2)$  with  $\lambda_3 = 1/(\lambda_1\lambda_2)$ . For clarity of visualization, the plot is shown only in the region between uniaxial tension  $\lambda_2 = \lambda_1^{-1/2} < 1$  and biaxial tension  $\lambda_2 = \lambda_1 > 1$ ; the complete plot follows from symmetry.

where, again,  $I_1 = \text{tr}(\mathbf{F}^T \mathbf{F})$  and  $I_2 = 1/2[I_1^2 - \text{tr}(\mathbf{F}^T \mathbf{F} \mathbf{F}^T \mathbf{F})]$  stand for the first and second principal invariants of the right Cauchy–Green deformation tensor  $\mathbf{C} = \mathbf{F}^T \mathbf{F}$ . Fig. 7 provides a plot of these sets of deformations in the projected space of principal stretches  $(\lambda_1, \lambda_2)$  with  $\lambda_3 = 1/(\lambda_1 \lambda_2)$ , where we recall the elementary connections  $I_1 = \lambda_1^2 + \lambda_2^2 + \lambda_3^2$  and  $I_2 = \lambda_1^2 \lambda_2^2 + \lambda_1^2 \lambda_3^2 + \lambda_2^2 \lambda_3^2$ . We therefore have

$$G_c = \begin{cases} G_c^a = 1000 \text{ N/m} & \text{if } (I_1, I_2) \in \mathcal{A} \\ G_c^{c_1} = 2500 \text{ N/m} & \text{if } (I_1, I_2) \in \mathcal{C}_1 \\ G_c^{c_2} = 10000 \text{ N/m} & \text{if } (I_1, I_2) \in \mathcal{C}_2 \end{cases} \quad (25)$$

for the critical energy release rate of elastomer D. By construction, the prescription (25) implies that under states of uniaxial tension the switch from  $G_c^a$  to  $G_c^{c_1}$  occurs at a stretch of  $\lambda_{ut}^{c_1} = 3.5$ , and from  $G_c^{c_1}$  to  $G_c^{c_2}$  at  $\lambda_{ut}^{c_2} = 4.5$ . Moreover, consistent with the recent experiments of Chen et al. (2019), the prescription (25) also entails that the switches from  $G_c^a$  to  $G_c^{c_1}$  and then from  $G_c^{c_1}$  to  $G_c^{c_2}$  take place at stretches that are increasingly larger for deformation states that approach equal biaxial tension.

**Remark 8.** Strain crystallization in natural rubber is a complex phase transition that is yet to be fully understood, especially the impact that it has on fracture properties. The simplistic piecewise constant description (25) for the critical energy release rate of elastomer D is, of course, not intended to capture the many intricacies associated with strain crystallization, such as the fact that the apparent critical energy release rate may be anisotropic or that its value increases monotonically with content of crystallinity, which itself depends strongly on the state of deformation. Such traverses notwithstanding, the description (25) does capture the basic feature associated with strain crystallization: *cracks encounter a larger resistance to propagate in strain-crystallized rubber than in amorphous rubber, more so the larger the degree of crystallinity*. As will become apparent below in the comparisons with the experiments, the piecewise constant description (25) is all we need for our purposes here.

### 5. Theory vs. experiments

We are now in a position to deploy the fracture theory (4)–(5), specialized to the stored-energy function (7) with material parameters (15), external driving force (10) with stochastic hydrostatic strength in the range (17), and critical energy release rate (25), to examine the poker-chip experiments of Gent and Lindley (1959).

In all the simulations that follow,  $\eta_W = 10^{-3}$ ,  $\eta_\kappa = (\mu/\kappa)10^{-3} = 2.67 \times 10^{-7}$ , and the localization length is set to the sufficiently small value of  $\epsilon = 30 \mu\text{m}$ . Exploiting symmetry, depending on the specimen initial thickness  $H$ , the simulations are carried out over an octant, a quarter, or a half of the specimens. The results are generated with the FE scheme presented in Section 4 of Kumar et al. (2018a) by making use of uniform unstructured meshes of size  $h = \epsilon/3 = 10 \mu\text{m}$ . Moreover, for each poker-chip test that is examined, simulations are carried out for at least two different realizations of spatial stochasticity of the hydrostatic strength  $s_{hs}$ .

We begin in Section 5.1 by comparing the force-deformation response predicted by the theory with the experimental response of three representative specimens – ranging from very thin, to thin, to thick in initial thickness  $H$  – extracted from the results reported by Gent and Lindley (1959) in Fig. 1 of their paper. We devote Sections 5.2 and 5.3 to comparing the predictions from the theory with the post-mortem images of the midplane of the specimens and with the experimental values of the “local-maximum stress”  $S'$  extracted, respectively, from Figs. 4 and 6 of their paper.

#### 5.1. The force-deformation response

*A very thin poker-chip specimen:*  $H = 0.056 \text{ cm}$ . Figs. 8(a)–(b) confront the force-deformation response predicted by the theory (solid line) with the experimental data (dotted line) for a very thin poker-chip specimen with initial thickness  $H = 0.056 \text{ cm}$ ; whereas part (a) shows the results in the entire range of reported applied deformations  $\lambda = h/H \in [1, 6.25]$ , part (b) zooms in the small-deformation region  $\lambda \in [1, 1.20]$ . To gain precise insight into the results, Fig. 8(c) also shows contour plots predicted by the theory for the phase field  $z$  and the regions of the elastomer that undergo strain crystallization at four applied deformations,  $\lambda = 1.02, 1.20, 2.00$ , and 5.00. The phase field  $z$  is shown both from a 3D perspective over an octant of the specimen and over its midplane. The results for strain crystallization are shown just over an octant.

Two observations from Figs. 8(a)–(b) are noteworthy. First, the theory is in fairly good quantitative agreement with the experiment. Second, the response shows three distinct successive regions:

- an approximately linear response from  $\lambda = 1$  up to about  $\lambda = 1.01$ ,
- a rugged plateau from  $\lambda = 1.01$  up to about  $\lambda = 2.00$ , and
- a nonlinear stiffening response from  $\lambda = 2.00$  up to  $\lambda = 6.25$ .

As can be deduced from the contour plots of the phase field  $z$  in Fig. 8(c), the initial approximately linear response of the specimen is due solely to the elastic deformation of the elastomer.

At about  $\lambda = 1.01$ , a plurality of cracks nucleate around the center of the specimen. They are all roughly of the same penny-shaped geometry. Upon further loading, the nucleated cracks exhibit limited propagation, instead, they mostly deform and more cracks of the same penny-shaped geometry are nucleated at adjacent locations on and around the midplane of the specimen. The nucleation of new adjacent cracks together with the limited propagation of all previously nucleated cracks continues until the entire midplane of the specimen – save for a boundary layer surrounding its free edge – is substantially populated with cracks. The rugged plateau region in the force-deformation response is precisely the result of this cascading process. Here, it is important to emphasize that

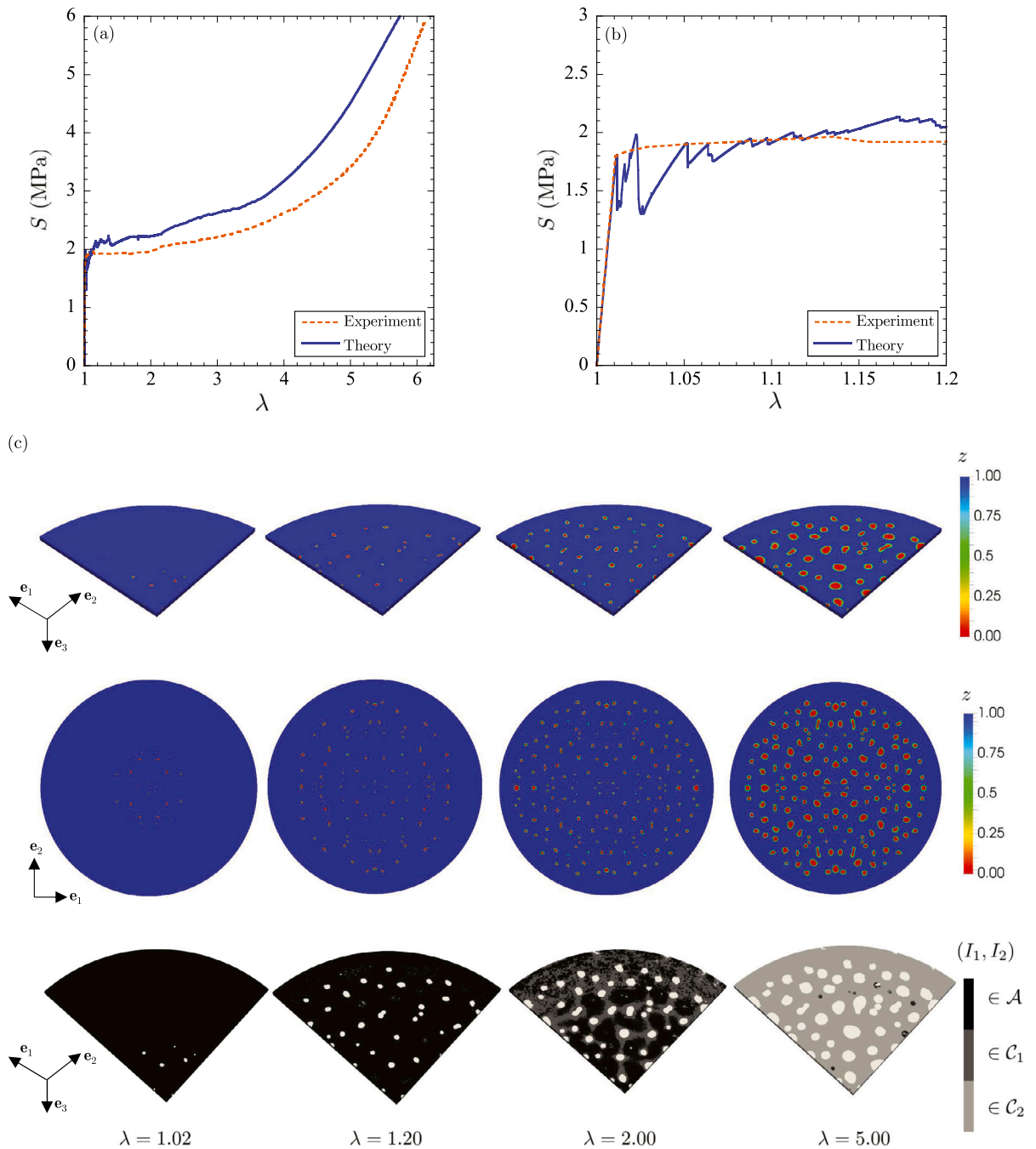


**Fig. 8.** Comparison between theory and experiment for the poker-chip test with initial thickness  $H = 0.056$  cm. (a) The normalized force  $S = 4P/(\pi D^2)$  as a function of the normalized applied deformation  $\lambda = h/H$ . (b) Close-up of the  $S$ - $\lambda$  response in the small-deformation region. (c) Contour plots, over the undeformed configuration, of the phase field  $z$  and the regions of the elastomer that undergo strain crystallization at four select applied deformations  $\lambda$ , as predicted by the theory.

the precise locations at which the cracks nucleate across the midplane are controlled by the stochasticity of the hydrostatic strength  $s_{hs}$  of the elastomer, thus different realizations of stochasticity lead to different results in terms of the locations of the cracks. The number of nucleated cracks and the loads at which they nucleate, however, are roughly the same for all realizations resulting thus in similar force–deformation responses; see [Appendix B](#).

The nonlinear stiffening in the force–deformation response that ensues after  $\lambda = 2.00$  is the manifestation of the facts that the nucleation of cracks slows down then and that the propagation of all the previously nucleated cracks still remains limited resulting

in the large stretching – and hence stiffening – of the portion of the elastomer that remains intact between the cracks. At about  $\lambda = 2.00$ , as illustrated by the third row of contour plots in Fig. 8(c), plenty of regions in the elastomer – in particular, the regions immediately ahead of the crack fronts (shown in white) – have reached deformations that are large enough ( $(I_1, I_2) \notin \mathcal{A}$ ) to strain crystallize. This further hinders the propagation of the cracks and further promotes the stiffening of the force-deformation response.

**Remark 9.** The ruggedness of the plateau region predicted by the theory is noticeably more pronounced than that of the experiment. A possible reason for this difference is that the theory does not account for the viscous dissipation in the rubber, which is expected to smoothen the force drops between nucleation events. Moreover, the spatial stochasticity of the hydrostatic strength might not have been isotropically distributed throughout the poker-chips, as assumed in the simulations, but, instead, anisotropically biased by their fabrication process. This is because anisotropic stochasticity would reduce the probability of simultaneous nucleation of multiple cracks and hence of the large force drops that they entail. Yet another possible reason is that the time resolution of the Hounsfield tensometer used by Gent and Lindley (1959) might not have been sufficiently high to capture the rapid change in force between nucleation events.

*A thin poker-chip specimen:*  $H = 0.183$  cm. Fig. 9 presents results entirely analogous to those shown in Fig. 8 for the case of a thicker but still relatively thin poker-chip specimen with initial thickness  $H = 0.183$  cm. The experimental force-deformation response shows the same three distinct regions as those shown by the very thin poker-chip specimen in Figs. 8(a) and (b). There are, however, quantitative differences all of which are explained and quantitatively captured by the theory.

First, the initial approximately linear response of the specimen extends from  $\lambda = 1$  to about  $\lambda = 1.06$ . Once more, as can be deduced from the contour plots of the phase field  $z$  in Fig. 9(c), this initial region in the force–deformation response is due solely to the elastic deformation of the elastomer.

At about  $\lambda = 1.06$ , three cracks nucleate near the top boundary of the specimen around its centerline – and *not* at the center of the specimen – and initially propagate *in the direction of the applied load* towards the bottom boundary. While one of them stops propagating upon further loading, the other two continue to do so and, after traversing almost the entire thickness of the specimen, proceed by propagating radially outwards in the direction of the free edge. At about  $\lambda = 1.16, 1.33$ , and  $2.30$  two, four, and then twelve more cracks are nucleated near the top boundary radially away from the centerline. Akin to the first nucleated cracks, the new cracks nucleated at  $\lambda = 1.16$  and  $1.33$  first propagate in the direction of the applied load and then proceed by propagating towards the free edge of the specimen. The rugged plateau spanning from  $\lambda = 1.06$  to about  $\lambda = 1.50$  in the force-deformation response is the result of such a string of succeeding crack nucleations and propagations. The cracks nucleated at  $\lambda = 2.30$  exhibit limited propagation upon further loading, but their sudden appearance shows up as a small drop in the force-deformation response.

At about  $\lambda = 2.50$ , the force-deformation response transitions into its final region of nonlinear stiffening. This is so because the nucleation of cracks has stopped by then and the propagation of all the nucleated cracks remains limited upon further loading. Also at about  $\lambda = 2.50$ , most portions of the elastomer around the cracks have reached large enough deformations ( $(I_1, I_2) \notin \mathcal{A}$ ) to strain crystallize. This makes the propagation of the cracks even more difficult and further promotes the stiffening of the force-deformation response.

**Remark 10.** A key difference between the responses of the poker-chip specimens with initial thicknesses  $H = 0.183$  cm and  $H = 0.056$  cm is that the nucleation of cracks occurs near the top boundary (and/or bottom boundary, depending on the stochasticity of the hydrostatic strength  $s_{hs}$ ) with the metal fixtures in the former and around the midplane of the specimen in the latter. One can understand this difference at once by recalling from Section 4.2 above that the strength of elastomer D is substantially weakest in hydrostatic tension and from Subsection 3.1 in (Lefèvre et al., 2015) that the hydrostatic stress in poker-chip specimens is always largest at the elastomer/fixtures interfaces — and *not* at the midplane of the poker-chip as often incorrectly stated in the literature. Accordingly, the nucleation of cracks is expected to occur near the top and/or bottom boundaries, where the hydrostatic stress first reaches values in the critical range (17) of the hydrostatic strength  $s_{hs}$ , in all poker-chip specimens of elastomer D, save for the very thin ones. This is because the stress field in the very thin poker-chip specimens is essentially uniform and hydrostatic throughout their thickness (see Fig. 5, for example) and, as a result, their midplane provides a more energetically favorable location for nucleation because it is farthest away from the rigidly constraining elastomer/fixtures interfaces; see Section 3.2 in Lefèvre et al. (2015) for a detailed analysis.

We remark, however, that if the elastomer being tested had uniaxial and biaxial tensile strengths comparable to its hydrostatic strength, the nucleation of cracks could take place in different locations of the poker-chip and *not* necessarily near the top and/or bottom boundaries. Section 5 in Kumar and Lopez-Pamies (2020) presents results for this very scenario on a soft silicone elastomer with  $s_{hs} = 0.50$  MPa,  $s_{ts} = 0.41$  MPa, and  $s_{bs} = 0.32$  MPa.

*A thick poker-chip specimen:*  $H = 0.365$  cm. Fig. 10 presents results analogous to those shown in Figs. 8 and 9 now for the case of a thick poker-chip specimen with initial thickness  $H = 0.365$  cm. The experimental force-deformation response features the same three distinct regions identified in those figures for the very thin and the thin poker-chip specimens, albeit with significant quantitative differences. All three regions remain well predicted by the theory.

Specifically, the initial response prior to the occurrence of fracture extends from  $\lambda = 1$  to about  $\lambda = 1.25$ . Because of the sizable deformations involved in this larger range, the  $S$ - $\lambda$  response exhibits some nonlinearity beyond  $\lambda = 1.10$  due to the nonlinear elasticity of the elastomer.

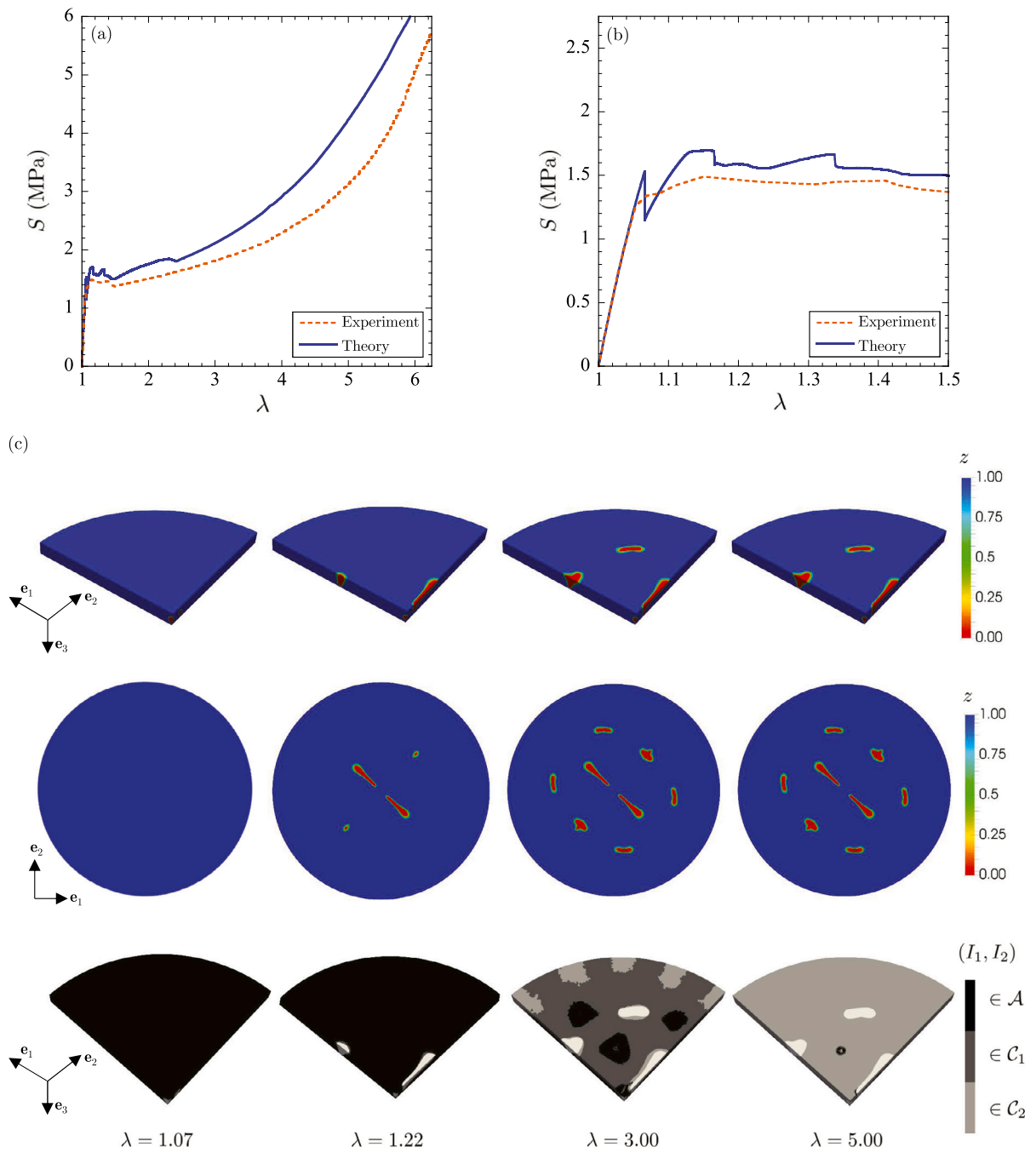


Fig. 9. Comparison between theory and experiment for the poker-chip test with initial thickness  $H = 0.183$  cm. (a) The normalized force  $S = 4P/(\pi D^2)$  as a function of the normalized applied deformation  $\lambda = h/H$ . (b) Close-up of the  $S$ - $\lambda$  response in the small-deformation region. (c) Contour plots, over the undeformed configuration, of the phase field  $z$  and the regions of the elastomer that undergo strain crystallization at four select applied deformations  $\lambda$ , as predicted by the theory.

At about  $\lambda = 1.25$ , a single crack nucleates near the top boundary of the specimen around its centerline. Upon further loading, the crack propagates first towards the bottom boundary and, after traversing almost the entire thickness of the specimen, radially outwards in the direction of the free edge. In this case, since no more cracks are nucleated, the rugged plateau ranges only from  $\lambda = 1.25$  to about  $\lambda = 1.30$  and is the result of the nucleation of the crack and its propagation towards the opposite boundary.

The nonlinear stiffening region begins at  $\lambda = 1.30$ , when the crack starts propagating radially outwards but it does so slowly enough that the stiffening due to the deformation of the elastomer translates directly into the stiffening of the force-deformation

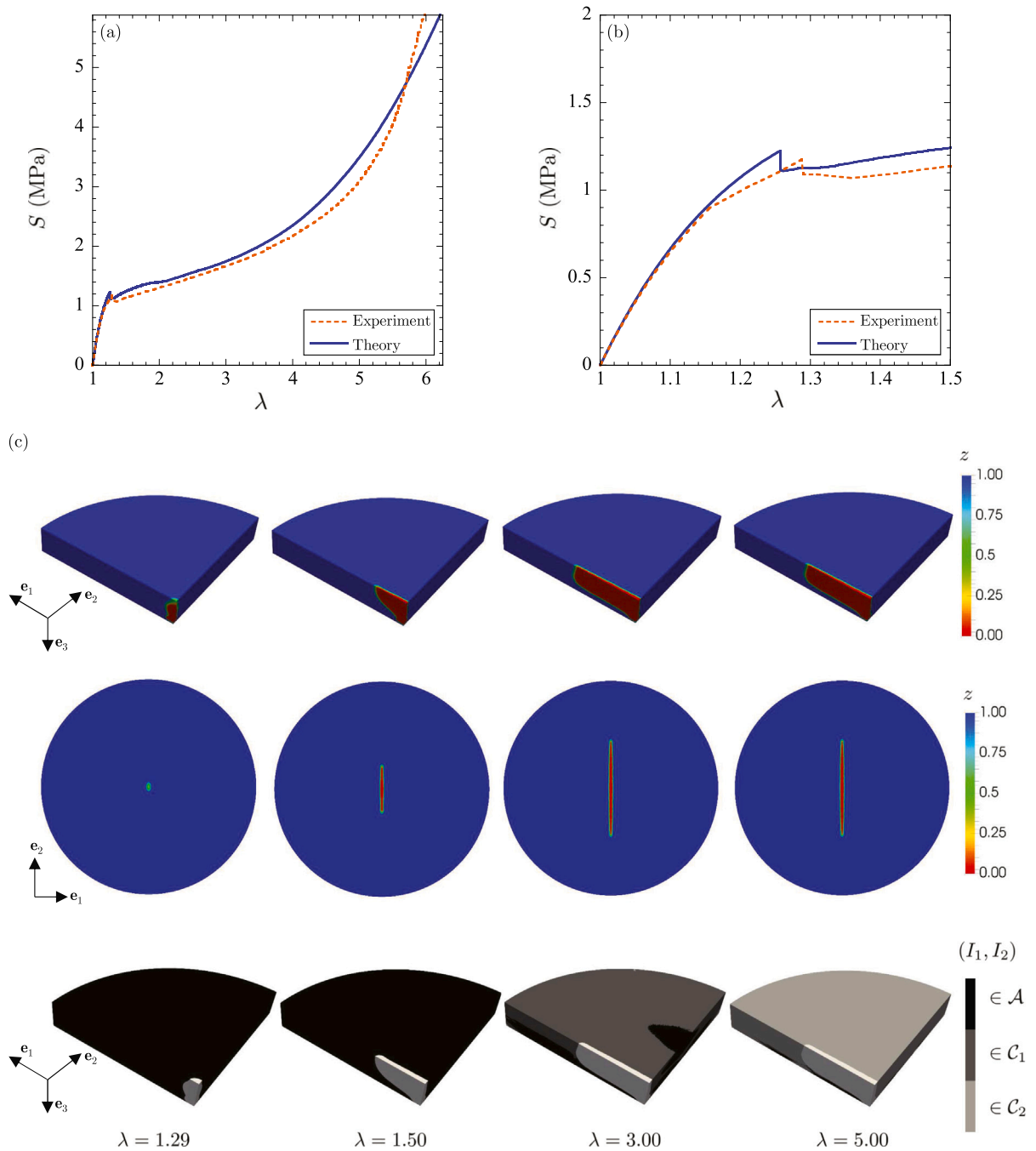


Fig. 10. Comparison between theory and experiment for the poker-chip test with initial thickness  $H = 0.365$  cm. (a) The normalized force  $S = 4P/(\pi D^2)$  as a function of the normalized applied deformation  $\lambda = h/H$ . (b) Close-up of the  $S$ - $\lambda$  response in the small-deformation region. (c) Contour plots, over the undeformed configuration, of the phase field  $z$  and the regions of the elastomer that undergo strain crystallization at four select applied deformations  $\lambda$ , as predicted by the theory.

response of the specimen. By  $\lambda = 3.00$ , plenty of portions of the elastomer have reached large enough deformations ( $(I_1, I_2) \notin \mathcal{A}$ ) to strain crystallize. Similar to the two preceding thinner specimens, this makes the propagation of the crack even more difficult and further promotes the stiffening of the force-deformation response.

We close this subsection by noting that the files MH056midun, MH056middef, MH183midun, MH183middef, MH365midun, MH365middef in the supplementary material provide videos of the simulations shown in Figs. 8 through 10 over the midplane of the specimens in the undeformed and deformed configurations.

5.2. The geometry and spatial distribution of the cracks across the midplane

Fig. 11 confronts the contour plots of the phase field  $z$  predicted by the theory with the post-mortem images of the midplane of poker-chip specimens cut open after reaching a normalized force of  $S = 2.75$  MPa. The results correspond to specimens with initial thicknesses ranging from the very thin to the thick,  $H = 0.061, 0.180, 0.295,$  and  $0.370$  cm. Consistent with the experiment, the contour plots of the phase field  $z$  are shown over the undeformed configuration of the specimens.

In addition to the good agreement between the theory and experiment, two other immediate observations from Fig. 11 are that:

- the penny-shaped geometry of the cracks in the thinnest specimen ( $H = 0.061$  cm) is different from the elongated geometry of the cracks in the other three specimens ( $H = 0.0180, 0.295, 0.370$  cm), and
- the number of cracks increases with decreasing initial thickness  $H$ .

As gathered from the preceding subsection, the penny-shaped geometry of the cracks in the thinnest specimen owes its origin to the fact that they nucleate around the midplane of the specimen, rather than nucleating near the boundaries with the metal fixtures (and then propagating through the thickness, traversing the midplane, and succeedingly radially outwards) as the cracks in the other three specimens with larger initial thicknesses.

As also gathered from the preceding subsection, the number of nucleated cracks scales *grosso modo* with the volume fraction of elastomer that reaches values of hydrostatic stress in the critical range (17) of the hydrostatic strength  $s_{hs}$ . Since larger volume fractions of elastomer reach such values of hydrostatic stress in thinner specimens, a larger number of cracks nucleate in thinner specimens.

We emphasize once more that the precise locations at which the cracks nucleate, around the midplane in very thin specimens or near the top and bottom boundaries in thicker specimens, depend on the stochasticity of the hydrostatic strength  $s_{hs}$  of the elastomer. In other words, different realizations of stochasticity lead to different results in terms of the locations of the cracks. The number of nucleated cracks, however, is *not* fundamentally different for different realizations and neither is the fact that cracks first nucleate around the centerline of the specimens while succeeding nucleations mostly occur radially outwards. Thus, much like their experimental counterparts, the theoretical results presented in Fig. 11, which correspond to one particular realization of stochasticity for each initial thickness  $H$ , can be viewed as representative of other realizations for specimens with the same  $H$ .

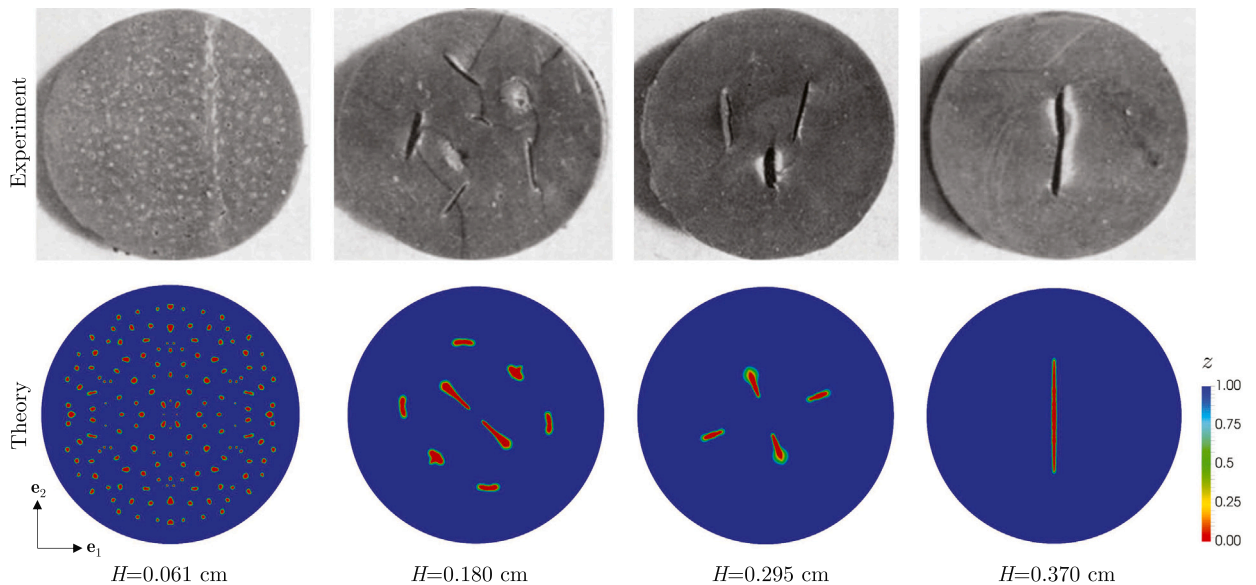


Fig. 11. Comparison between theory and experiment for the post-mortem images of the midplane of poker-chip specimens – cut open after reaching a normalized force of  $S = 2.75$  MPa – with four increasing initial thicknesses  $H$ .

5.3. The “local-maximum stress”  $S'$  as a function of poker-chip initial thickness  $H$

Fig. 12 confronts the “local-maximum stress”  $S'$  predicted by the theory (solid line) with the experimental data (solid circles) for poker-chip specimens with initial thicknesses ranging from  $H = 0.040$  cm to  $H = 0.496$  cm; recall that  $S'$  stands for the value of the normalized force  $S$  at the first local maximum in the force-deformation response of the specimens. The error bars in the theoretical results span the range of values obtained from all the different realizations of stochasticity of the hydrostatic strength  $s_{hs}$  that were investigated.

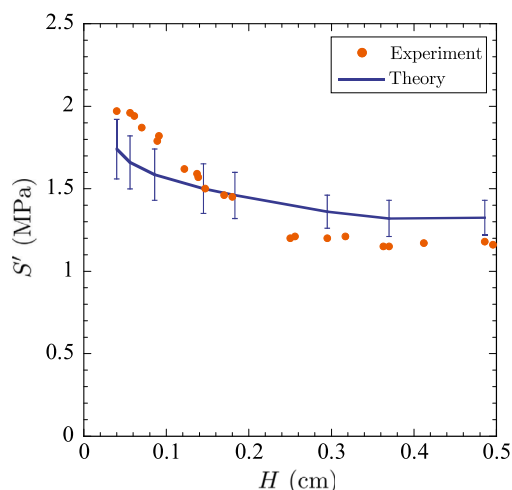


Fig. 12. Comparison between theory and experiment for the “local-maximum stress”  $S'$  as a function of the initial thickness  $H$  of the poker-chip specimens.

As was the case for the two preceding sets of comparisons, the theory is in fairly good quantitative agreement with the experiment. It is also noteworthy that the value of  $S'$  decreases with increasing initial thickness  $H$ . This trend is the manifestation of the fact that thinner specimens require larger normalized forces  $S$  to reach hydrostatic stresses within the elastomer (because of its near incompressibility) in the critical strength range (17).

## 6. Final comments

In a nutshell, the results presented in Section 5 have established that:

- i. the nucleation of cracks in the poker-chip experiments of Gent and Lindley (1959) is governed by the strength – in particular, the hydrostatic strength – of the elastomer, while
- ii. the propagation of the nucleated cracks is governed by the Griffith competition between the bulk elastic energy of the elastomer and its surface fracture energy.

As alluded to in the Introduction, one of the reasons why it has taken six decades to finally reach this seemingly simple explanation is that the *approximate*<sup>12</sup> elasticity analysis of the nucleation of internal cracks – that is, again, cavitation – proposed by Gent and Lindley (1959) turned out to be in reasonable agreement with some of the values that they measured for the “local-maximum stress”  $S'$ . Gent and Lindley (1959) posited their elasticity view in part because they found experimentally that  $S'$  depended approximately linearly on the Young’s modulus  $E$  of the elastomers that they investigated, this for any of the initial thicknesses  $H$  of the poker-chip specimens that they considered; Fig. 7 of their paper shows a representative plot of  $S'$  for poker-chip specimens with initial thickness  $H = 0.3$  cm as an approximately linear function of  $E$  from  $E = 0.932$  to 5.884 MPa. This was an unfortunate misleading coincidence that now, in view of the results in Section 5, can be easily explained.

**Table 1**  
Hydrostatic strength for the five different types of unfilled elastomers investigated by Gent and Lindley (1959).

Elastomer	$E$ (MPa)	$s_{\text{hs}}$ (MPa)	$s_{\text{hs}}/E$
D	1.765	$2.9 \pm 0.5$	$1.64 \pm 0.24$
E	1.255	$2.4 \pm 0.4$	$1.91 \pm 0.32$
F	1.196	$2.3 \pm 0.6$	$1.92 \pm 0.50$
G	0.981	$1.9 \pm 0.3$	$1.94 \pm 0.31$
H	0.932	$1.9 \pm 0.3$	$2.04 \pm 0.32$

Table 1 lists the values of the hydrostatic strength  $s_{\text{hs}}$  for the unfilled elastomers E, F, G, H investigated by Gent and Lindley (1959), as extracted<sup>13</sup> from the values of the “local-maximum stress”  $S'$  that they plotted in Fig. 6 of their paper; the corresponding

<sup>12</sup> When the elasticity analysis is carried out more accurately by resolving numerically the local deformation and stress fields in the specimens, the quantitative agreement with the experiments turns out to be less favorable; see Fig. 14(b) in Lefèvre et al. (2015).

<sup>13</sup> In an entirely analogous manner to the elastic calculations presented in Section 4.2 above, the values of  $s_{\text{hs}}$  are obtained by first reproducing theoretically the pertinent poker-chip experiments under the premise that the elastomers are only capable of deforming elastically – their elasticity being characterized by incompressible Neo-Hookean behavior with the initial Young’s modulus  $E$  reported by Gent and Lindley (1959) in Table 1 of their paper – and by then identifying

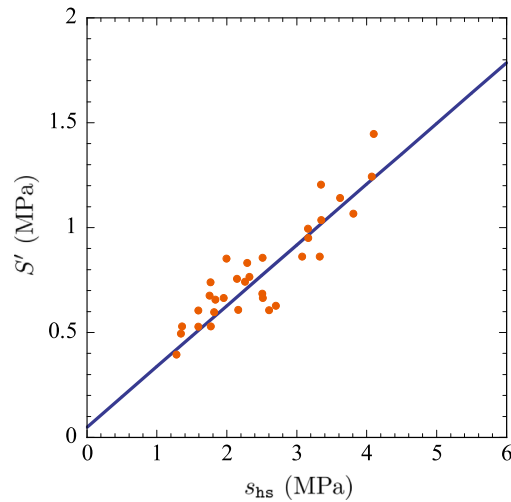


Fig. 13. Relation between the “local-maximum stress”  $S'$  and the hydrostatic strength  $s_{hs} = 1.9E$  for poker-chip specimens with initial thickness  $H = 0.3$  cm, reproduced from Fig. 7 in Gent and Lindley (1959).

value (17) for elastomer D is also included in the table for direct comparison. The last column of the table provides the hydrostatic-strength-to-Young’s-modulus ratio  $s_{hs}/E$ . Remarkably, this ratio is roughly the same for each of the five different types of elastomers, namely, about  $s_{hs}/E = 1.9$ . Thus, the observation made by Gent and Lindley (1959) that  $S'$  depended approximately linearly on the Young’s modulus  $E$  of the elastomers had little to do with their initial elasticity and much to do with the fact that, coincidentally, the hydrostatic strength  $s_{hs}$  was given by roughly the same multiple 1.9 of  $E$  for all the elastomers that were investigated. Fig. 13 reproduces the data from Fig. 7 in their paper for elastomers D, E, F, G, H, now plotted as a function of the hydrostatic strength  $s_{hs} = 1.9E$  instead of the Young’s modulus  $E$ , to convey this point pictorially. The solid line in the figure corresponds to the heuristic formula  $S' = 0.55E + 0.049 = 0.29s_{hs} + 0.049$  proposed by Gent and Lindley (1959), rewritten here in MPa and in terms of  $s_{hs}$ , to fit the experimental data (solid circles).

From a more general perspective, the results presented in Section 5 have also served to provide further validation to continue investigating the theory (4)–(5) as an appropriate *macroscopic* framework for the description of the nucleation and propagation of fracture in elastomers undergoing arbitrarily large quasistatic deformations.

We close by reiterating, nonetheless, that little remains known about the nucleation and propagation of fracture in elastomers from a *microscopic* point of view. A key open problem directly related to the results presented here is how to properly define microscopic defects, both geometrically and constitutively, as well as how to describe and upscale their growth to their macroscopic manifestation: the strength. The connections in Table 1 may have offered a clue by suggesting that the hydrostatic strength  $s_{hs}$  of elastomers is proportional to their cross-link density since, as is well known,  $E = 3NkT$  to a first approximation, where  $N$  stands for the number of chains per unit volume,  $k$  denotes the Boltzmann constant, and  $T$  is the absolute temperature; see, e.g., Chapter 4 in the monograph by Treloar (1975). The techniques presented in Gloria et al. (2014) and Cicalese et al. (2020) may be relevant in that pursuit.

#### CRediT authorship contribution statement

**Aditya Kumar:** Conceptualization, Methodology, Software, Writing - review & editing. **Oscar Lopez-Pamies:** Conceptualization, Methodology, Supervision, Writing - original draft, Writing - review & editing, Funding acquisition.

#### Declaration of competing interest

The authors declare that they have no known competing financial interests or personal relationships that could have appeared to influence the work reported in this paper.

#### Acknowledgment

This work was supported by the National Science Foundation, United States through the Grants DMS-1615661 and CMMI-1901583. This support is gratefully acknowledged.

---

as the hydrostatic strength the value of hydrostatic stress at the elastomer/fixtures boundaries along the centerline of the poker-chips when the normalized force  $S$  reaches the critical value  $S'$ . We use the value of  $S'$ , as opposed to  $S^*$ , since that is the only data that was provided by Gent and Lindley (1959). Accordingly, given that  $S' \geq S^*$ , the values of the hydrostatic strength  $s_{hs}$  in Table 1 for elastomers E, F, G, H are expected to be slightly larger than the actual ones.

## Appendix A. On the choice of piecewise constant critical energy release rate (25)

As remarked in the main body of the text, our choice of piecewise constant critical energy release rate (25) to model the effects of strain crystallization in the propagation of cracks in elastomer D is driven mostly by simplicity. Prior to settling on (25), we investigated the use of even simpler prescriptions.

First, we investigated the use of a constant critical energy release rate. Since the value of  $G_c = 1000$  N/m is needed to have agreement with the experiment on the specimen with initial thickness  $H = 0.370$  cm (see Fig. 11), we explored the use of this constant value for all simulations. The results turned out to be inconsistent with the experimental observations most notably in that they did not describe the latter stiffening of the force-deformation responses. A result illustrating such a disagreement is shown in Fig. 14 for the case of the poker-chip test with initial thickness  $H = 0.056$  cm.

Second, we investigated the use of a piecewise constant critical energy release rate with two branches. While this prescription led to results that could describe the latter stiffening of the force-deformation responses observed in the experiments, it could not describe at the same time the preceding plateau regions. A result illustrating this limitation is also shown in Fig. 14 for a piecewise constant critical energy release rate with values  $G_c = 1000$  N/m if  $(I_1, I_2) \in \mathcal{A}$  and  $G_c = 10000$  N/m if  $(I_1, I_2) \in C_1 \cup C_2$ .

At last, we investigated the use of a piecewise constant critical energy release rate with three branches, which proved capable of leading to agreement with the experiments. We emphasize that the specific values  $G_c = 1000, 2500$ , and  $10000$  N/m and the amorphous (22) and crystalline (23)–(24) regions were finally selected in the prescription (25) not only because they led to reasonable agreement with all the poker-chip experiments, but also because they are consistent with the experiments of Lake and Lindley (1965) and Chen et al. (2019).

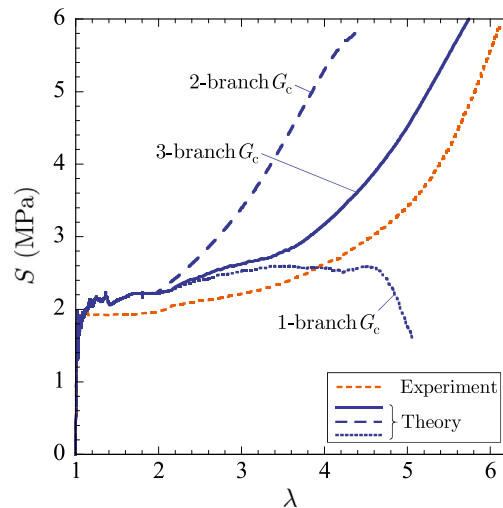


Fig. 14. Comparison between the theoretical predictions for three different prescriptions of the critical energy release rate  $G_c$  for the poker-chip test with initial thickness  $H = 0.056$  cm. The results show the normalized force  $S = 4P/(\pi D^2)$  as a function of the normalized applied deformation  $\lambda = h/H$  and pertain to: (i) the constant  $G_c = 1000$  N/m (labeled 1-branch  $G_c$ ), (ii) the piecewise constant  $G_c = 1000$  N/m if  $(I_1, I_2) \in \mathcal{A}$  and  $G_c = 10000$  N/m if  $(I_1, I_2) \in C_1 \cup C_2$  (labeled 2-branch  $G_c$ ), and (iii) the piecewise constant (25) used in the main body of the text (labeled 3-branch  $G_c$ ). The experimental result is also plotted for direct comparison.

## Appendix B. On the effects of the stochasticity of the hydrostatic strength (17)

For completeness, Fig. 15 provides a representative comparison between the predictions generated from the theory for two different realizations of stochasticity of the hydrostatic strength  $s_{hs}$ . The results pertain to the same poker-chip test with initial thickness  $H = 0.056$  cm examined in Fig. 8. As discussed in the main body of the text, the stochasticity controls the precise locations where cracks nucleate, but it has a minor effect on the number of nucleated cracks, on the loads at which they nucleate, and on the resulting force-deformation response of the specimen.

## Appendix C. Supplementary data

Supplementary material related to this article can be found online at <https://doi.org/10.1016/j.jmps.2021.104359>.

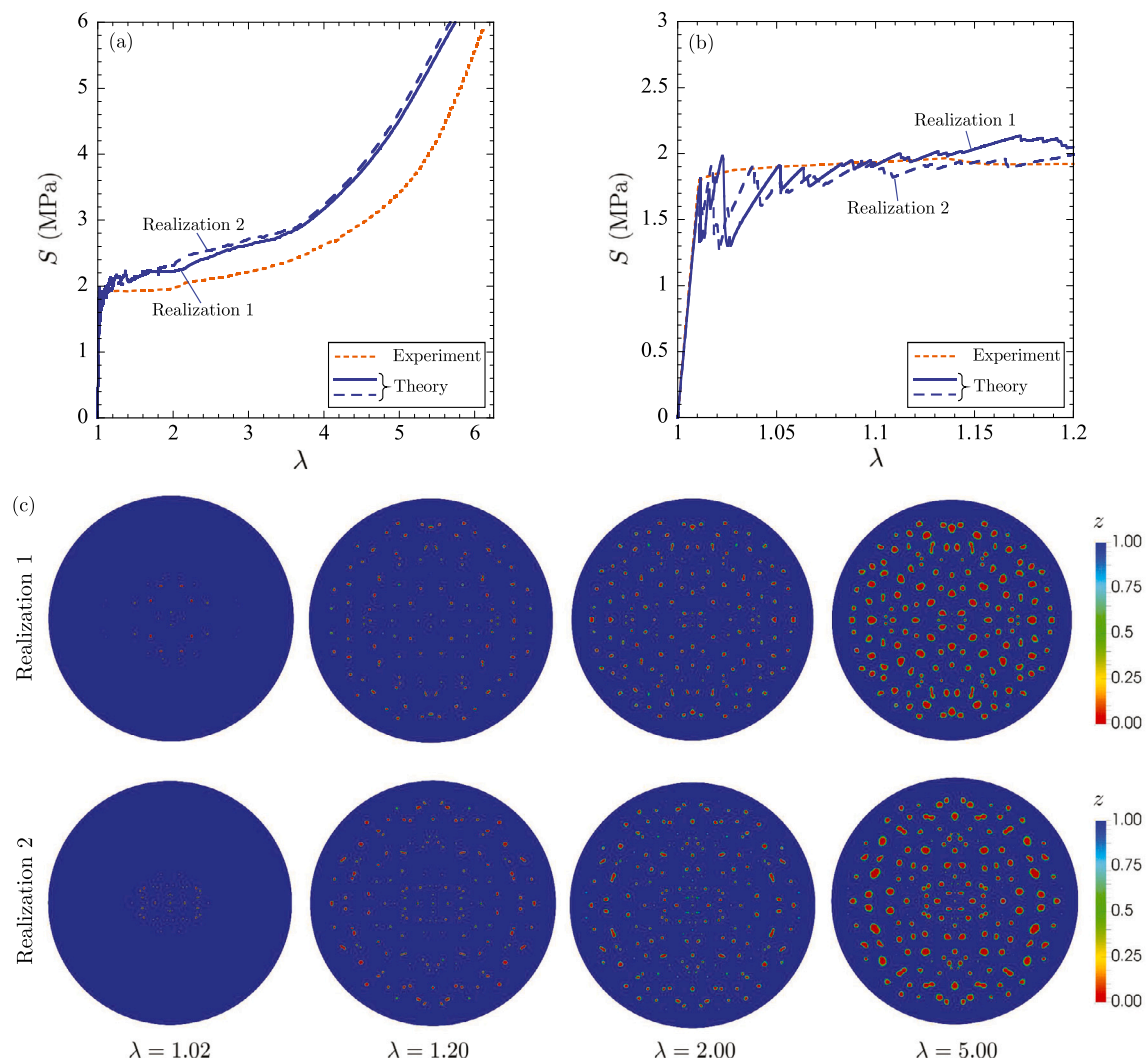


**Fig. 15.** Comparison between the theoretical predictions for two realizations of stochasticity of the hydrostatic strength  $s_{hs}$  for the poker-chip test with initial thickness  $H = 0.056$  cm. (a) The normalized force  $S = 4P/(\pi D^2)$  as a function of the normalized applied deformation  $\lambda = h/H$ . (b) Close-up of the  $S$ - $\lambda$  response in the small-deformation region. (c) Contour plots of the phase field  $z$  over the midplane of the specimens (in the undeformed configurations) at four select applied deformations  $\lambda$ . The experimental result is also included in parts (a) and (b) for direct comparison.

## References

- Ambrosio, L., Tortorelli, V.M., 1992. On the approximation of free discontinuity problems. *Boll. Unione Mat. Ital.* 6B, 105–123.
- Amor, H., Marigo, J.J., Maurini, C., 2009. Regularized formulation of the variational brittle fracture with unilateral contact: Numerical experiments. *J. Mech. Phys. Solids* 57, 1209–1229.
- Babuska, I., Zlamal, M., 1973. Nonconforming elements in the finite element method with penalty. *SIAM J. Numer. Anal.* 10, 863–875.
- Ball, J.M., 1982. Discontinuous equilibrium solutions and cavitation in nonlinear elasticity. *Phil. Trans. R. Soc. A* 306, 557–611.
- Behrman, W., 1998. An Efficient Gradient Flow Method for Unconstrained Optimization (Ph.D. thesis). Stanford University.
- Beurrot, S., Huneau, B., Verron, E., 2011. Strain-induced crystallization of natural rubber subjected to biaxial loading conditions as revealed by X-ray diffraction. In: *Proceedings of the 7th European Conference on Constitutive Models for Rubber*, pp. 23–28.
- Bourdin, B., Francfort, G.A., Marigo, J.J., 2008. The variational approach to fracture. *J. Elasticity* 91, 5–148.
- Bull, T.H., 1956. XIII. The tensile strengths of liquids under dynamic loading. *Phil. Mag.* 1, 153–165.
- Busse, W.F., 1934. Tear resistance and structure of rubber. *Ind. Eng. Chem.* 26, 1194–1199.
- Busse, W.F., 1938. Physics of rubber as related to the automobile. *J. Appl. Phys.* 9, 438–451.
- Chen, X., Meng, L., Zhang, W., Ye, K., Xie, C., Wang, D., Chen, W., Nan, M., Wang, S., Li, L., 2019. Frustrating strain-induced crystallization of natural rubber with biaxial stretch. *ACS Appl. Mater. Interfaces* 11, 47535–47544.
- Cicalese, M., Gloria, A., Ruf, M., 2020. From statistical polymer physics to nonlinear elasticity. *Arch. Ration. Mech. Anal.* 236, 1127–1215.
- Creton, C., Ciccotti, M., 2016. Fracture and adhesion of soft materials: a review. *Rep. Progr. Phys.* 79, 046601.
- Crouzeix, M., Raviart, P.-A., 1973. Conforming and nonconforming finite element methods for solving the stationary Stokes equations I. *Rev. Française Automat. Informat. Recherche Opérationnelle* 7, 33–75.

- Del Piero, G., Lancioni, G., March, R., 2007. A variational model for fracture mechanics: Numerical experiments. *J. Mech. Phys. Solids* 55, 2513–2537.
- Dickie, R.A., Smith, T.L., 1969. Ultimate tensile properties of elastomers. VI. Strength and extensibility of a styrene-butadiene rubber vulcanizate in equal biaxial tension. *J. Polym. Sci. A-2 Polym. Phys.* 7, 687–707.
- Flory, P.J., 1947. Thermodynamics of crystallization in high polymers. I. Crystallization induced by stretching. *J. Chem. Phys.* 15, 397–408.
- Fond, C., 2001. Cavitation criterion for rubber materials: A review of void-growth models. *J. Polym. Sci. Part B* 39, 2081–2096.
- Francfort, G.A., Giacomini, A., Lopez-Pamies, O., 2019. Fracture with healing: a first step towards a new view of cavitation. *Anal. PDE* 12, 417–447.
- Francfort, G.A., Marigo, J.J., 1998. Revisiting brittle fracture as an energy minimization problem. *J. Mech. Phys. Solids* 46, 1319–1342.
- Fried, E., Gurtin, M.E., 1994. Dynamic solid–solid transitions with phase characterized by an order parameter. *Physica D* 72, 287–308.
- Gent, A.N., 1958. On the relation between indentation hardness and Young's modulus. *Rubber Chem. Technol.* 31, 896–906.
- Gent, A.N., 1990. Cavitation in rubber: a cautionary tale. *Rubber Chem. Technol.* 63, G49–G53.
- Gent, A.N., Lindley, P.B., 1957. Internal flaws in bonded cylinders of soft vulcanized rubber subjected to tensile loads. *Nature* 180, 912–913.
- Gent, A.N., Lindley, P.B., 1959. Internal rupture of bonded rubber cylinders in tension. *Proc. R. Soc. Lond. Ser. A Math. Phys. Eng. Sci.* 249, 195–205.
- Gent, A.N., Mars, W.V., 2013. Strength of elastomers. In: Mark, J.E., Erman, B., Roland, C.M. (Eds.), *The Science and Technology in Rubber*. Elsevier.
- Gent, A.N., Park, B., 1984. Failure processes in elastomers at or near a rigid inclusion. *J. Mater. Sci.* 19, 1947–1956.
- Gent, A.N., Wang, C., 1991. Fracture mechanics and cavitation in rubber-like solids. *J. Mater. Sci.* 26, 3392–3395.
- Gloria, A., Le Tallec, P., Vidrascu, M., 2014. Foundation, analysis, and numerical investigation of a variational network-based model for rubber. *Continuum Mech. Thermodyn.* 26, 1–31.
- Griffith, A.A., 1921. The phenomena of rupture and flow in solids. *Philos. Trans. R. Soc. Lond. Ser. A* 221, 163–198.
- Gullié, J., Thien-Nga, L., Le Tallec, P., 2015. Micro-sphere model for strain-induced crystallisation and three-dimensional applications. *J. Mech. Phys. Solids* 81, 58–74.
- Gurtin, M.E., 1996. Generalized Ginzburg-Landau and Cahn-Hilliard equations based on a microforce balance. *Physica D* 92, 178–192.
- Hamed, G.R., Kim, H.J., Gent, A.N., 1996. Cut growth in vulcanizates of natural rubber, cis-polybutadiene, and a 50-50 blend during single and repeated extension. *Rubber Chem. Technol.* 69, 807–818.
- Hansbo, P., Larson, M.G., 2003. Discontinuous Galerkin and the Crouzeix–Raviart element: Application to elasticity. *Math. Model. Numer. Anal.* 37, 63–72.
- Henaó, D., Mora-Corral, C., Xu, X., 2016. A numerical study of void coalescence and fracture in nonlinear elasticity. *Comput. Methods Appl. Mech. Engrg.* 303, 163–184.
- Hesch, C., Weinberg, K., 2014. Thermodynamically consistent algorithms for a finite-deformation phase-field approach to fracture. *Internat. J. Numer. Methods Engrg.* 99, 906–924.
- Hocine, N.A., Abdelaziz, M.N., Imad, A., 2002. Fracture problems of rubbers: *J*-integral estimation based upon  $\eta$  factors and an investigation on the strain energy density distribution as a local criterion. *Int. J. Fract.* 117, 1–23.
- Horgan, C.O., Polignone, D.A., 1995. Cavitation in nonlinearly elastic solids: A review. *Appl. Mech. Rev.* 48, 471–485.
- Huneau, B., 2011. Strain-induced crystallization of natural rubber: A review of X-ray diffracton investigations. *Rubber Chem. Technol.* 84, 425–452.
- Katz, J.R., 1925. Röntgenspektrographische untersuchungen am gedehnten kautschuk und ihre mögliche Bedeutung für das problem der dehnungseigenschaften dieser substanz [X-ray spectrographic investigations on stretched rubber and their possible significance for the problem of the stretch properties of this substance]. *Naturwissenschaften* 13, 410–416.
- Kawabata, S., 1973. Fracture and mechanical behavior of rubber-like polymers under finite deformation in biaxial stress field. *J. Macromol. Sci. Part B* 8, 605–630.
- Kumar, A., Aranda-Iglesias, D., Lopez-Pamies, O., 2017. Some remarks on the effects of inertia and viscous dissipation in the onset of cavitation in rubber. *J. Elasticity* 126, 201–213.
- Kumar, A., Francfort, G.A., Lopez-Pamies, O., 2018a. Fracture and healing of elastomers: A phase-transition theory and numerical implementation. *J. Mech. Phys. Solids* 112, 523–551.
- Kumar, A., Lopez-Pamies, O., 2020. The phase-field approach to self-healable fracture of elastomers: A model accounting for fracture nucleation at large, with application to a class of conspicuous experiments. *Theor. Appl. Fract. Mech.* 107, 102550.
- Kumar, A., Ravi-Chandar, K., Lopez-Pamies, O., 2018b. The configurational-forces view of fracture and healing in elastomers as a phase transition. *Int. J. Fract.* 213, 1–16.
- Lake, G.J., Lindley, P.B., 1965. The mechanical fatigue limit for rubber. *J. Appl. Polym. Sci.* 9, 1233–1251.
- Lake, G.J., Thomas, A.G., 1967. The strength of highly elastic materials. *Proc. R. Soc. Lond. Ser. A Math. Phys. Eng. Sci.* 300, 108–119.
- Lefèvre, V., Ravi-Chandar, K., Lopez-Pamies, O., 2015. Cavitation in rubber: An elastic instability or a fracture phenomenon? *Int. J. Fract.* 192, 1–23.
- Leonard, M., Wang, N., Lopez-Pamies, O., Nakamura, T., 2020. The nonlinear elastic response of filled elastomers: Experiments vs. theory for the basic case of particulate fillers of micrometer size. *J. Mech. Phys. Solids* 135, 103781.
- Li, B., Bouklas, N., 2019. A variational phase-field model for brittle fracture in polydisperse elastomer networks. *Int. J. Solids Struct.* 182, 193–204.
- Lindsey, G.H., 1965. Hydrostatic Tensile Fracture of a Polyurathane Elastomer (Ph.D. thesis). California Institute of Technology.
- Lopez-Pamies, O., 2009. Onset of cavitation in compressible, isotropic, hyperelastic solids. *J. Elasticity* 94, 115–145.
- Lopez-Pamies, O., 2010. A new  $I_1$ -based model for rubber elastic materials. *Compt. R. Mec.* 338, 3–11.
- Lopez-Pamies, O., Idiart, M.I., Nakamura, T., 2011a. Cavitation in elastomeric solids: I — A defect-growth theory. *J. Mech. Phys. Solids* 59, 1464–1487.
- Lopez-Pamies, O., Nakamura, T., Idiart, M.I., 2011b. Cavitation in elastomeric solids: II — Onset-of-cavitation surfaces for neo-hookean materials. *J. Mech. Phys. Solids* 59, 1488–1505.
- Mandal, T.K., Gupta, A., Nguyen, V.P., Chowdhury, R., de Vaucorbeil, A., 2020. A length scale insensitive phase field model for brittle fracture of hyperelastic solids. *Eng. Fract. Mech.* 236, 107196.
- Miehe, C., Schänzel, L.M., 2014. Phase field modeling of fracture in rubbery polymers. Part I: Finite elasticity coupled with brittle failure. *J. Mech. Phys. Solids* 65, 93–113.
- Neuberger, J.W., 2010. *Sobolev Gradients and Differential Equations*. Springer, Heidelberg.
- Poulain, X., Lefèvre, V., Lopez-Pamies, O., Ravi-Chandar, K., 2017. Damage in elastomers: Nucleation and growth of cavities, micro-cracks, and macro-cracks. *Int. J. Fract.* 205, 1–21.
- Poulain, X., Lopez-Pamies, O., Ravi-Chandar, K., 2018. Damage in elastomers: Healing of internally nucleated cavities and micro-cracks. *Soft Matter* 14, 4633–4640.
- Raphaël, E., de Gennes, P.G., 1992. Rubber-rubber adhesion with connector molecules. *J. Phys. Chem.* 96, 4002–4007.
- Rivlin, R.S., Thomas, A.G., 1953. Rupture of rubber. Part I. Characteristic energy for tearing. *J. Polym. Sci.* 10, 291–318.
- Rong, G., Hamed, G.R., Jiang, J., 2016. Comparison of the strength of normal and edge-cut tensile specimens of styrene-butadiene rubber and natural rubber with similar crosslink density. *Rubber Chem. Technol.* 89, 631–639.
- Smith, T.L., 1964. Ultimate tensile properties of elastomers. II. Comparison of failure envelopes for unfilled vulcanizates. *J. Appl. Phys.* 35, 27–36.
- Smith, T.L., Rinde, J.A., 1969. Ultimate tensile properties of elastomers. V. Rupture in constrained biaxial tensions. *J. Polym. Sci. A-2 Polym. Phys.* 7, 675–685.
- Sotta, P., Albouy, P.-A., 2020. Strain-induced crystallization in natural rubber: Flory's theory revisited. *Macromolecules* 53, 3097–3109.
- Stringfellow, R., Abeyaratne, R., 1989. Cavitation in an elastomer: comparison of theory with experiment. *Mater. Sci. Eng. A* 112, 127–131.
- Talamini, B., Mao, Y., Anand, L., 2018. Progressive damage and rupture in polymers. *J. Mech. Phys. Solids* 111, 434–457.

- Tanné, E., Li, T., Bourdin, B., Marigo, J.J., Maurini, C., 2018. Crack nucleation in variational phase-field models of brittle fracture. *J. Mech. Phys. Solids* 110, 80–99.
- Thomas, A.G., 1994. The development of fracture mechanics for elastomers. *Rubber Chem. Technol.* 67, 50–67.
- Tosaka, M., Murakami, S., Poompradub, S., Kohjiya, S., Ikeda, Y., Toki, S., Sics, I., Hsiao, B.S., 2004. Orientation and crystallization of natural rubber network as revealed by WAXD using synchrotron radiation. *Macromolecules* 37, 3299–3309.
- Treloar, L.R.G., 1975. *The Physics of Rubber Elasticity*. Oxford University Press.
- Valentín, J.L., Posadas, P., Fernández-Torres, A., Malmierca, M.A., González, L., Chassé, W., Saalwächter, K., 2010. Inhomogeneities and chain dynamics in diene rubbers vulcanized with different cure systems. *Macromolecules* 43, 4210–4222.
- Williams, M.L., Schapery, R.A., 1965. Spherical flaw instability in hydrostatic tension. *Int. J. Fract. Mech.* 1, 64–72.
- Wood, L.A., Martin, G.M., 1964. Compressibility of natural rubber at pressures below 500 kg/cm<sup>2</sup>. *J. Res. Nat. Bureau Stand.* 68A, 259–268.
- Wu, J., McAuliffe, C., Waisman, H., Deodatis, G., 2016. Stochastic analysis of polymer composites rupture at large deformations modeled by a phase field method. *Comput. Methods Appl. Mech. Engrg.* 312, 596–634.
- Xu, X., Henaou, D., 2011. An efficient numerical method for cavitation in nonlinear elasticity. *Math. Models Methods Appl. Sci.* 21, 1733–1760.
- Yerzley, P.L., 1939. Adhesion of neoprene to metal. *Ind. Eng. Chem.* 31, 950–956.
- Zhang, H.P., Niemczura, J., Dennis, G., Ravi-Chandar, K., Marder, M., 2009. Toughening effect of strain-induced crystallites in natural rubber. *Phys. Rev. Lett.* 102, 245503.